Altered Ca^{2+} signaling in skeletal muscle fibers of the R6/2 mouse, a model of Huntington's disease

Peter Braubach,[1] Murat Orynbayev,[1] Zoita Andronache,[1] Tanja Hering,[1,2] Georg Bernhard Landwehrmeyer,[2] Katrin S. Lindenberg,[2] and Werner Melzer[1]

[1]Institute of Applied Physiology and [2]Department of Neurology, Ulm University, D-89081 Ulm, Germany

Huntington's disease (HD) is caused by an expanded CAG trinucleotide repeat within the gene encoding the protein huntingtin. The resulting elongated glutamine (poly-Q) sequence of mutant huntingtin (mhtt) affects both central neurons and skeletal muscle. Recent reports suggest that ryanodine receptor–based Ca^{2+} signaling, which is crucial for skeletal muscle excitation–contraction coupling (ECC), is changed by mhtt in HD neurons. Consequently, we searched for alterations of ECC in muscle fibers of the R6/2 mouse, a mouse model of HD. We performed fluorometric recordings of action potentials (APs) and cellular Ca^{2+} transients on intact isolated toe muscle fibers (musculi interossei), and measured L-type Ca^{2+} inward currents on internally dialyzed fibers under voltage-clamp conditions. Both APs and AP-triggered Ca^{2+} transients showed slower kinetics in R6/2 fibers than in fibers from wild-type mice. Ca^{2+} removal from the myoplasm and Ca^{2+} release flux from the sarcoplasmic reticulum were characterized using a Ca^{2+} binding and transport model, which indicated a significant reduction in slow Ca^{2+} removal activity and Ca^{2+} release flux both after APs and under voltage-clamp conditions. In addition, the voltage-clamp experiments showed a highly significant decrease in L-type Ca^{2+} channel conductance. These results indicate profound changes of Ca^{2+} turnover in skeletal muscle of R6/2 mice and suggest that these changes may be associated with muscle pathology in HD.

The Journal of General Physiology

INTRODUCTION

Huntington's disease (HD) is a monogenetic neurodegenerative disorder associated with characteristic hyperkinetic motoric dysfunction (chorea) accompanied by cognitive and emotional deficits (Cepeda et al., 2007; Imarisio et al., 2008; Miller and Bezprozvanny, 2010). The disease is of autosomal dominant inheritance and results from an expanded CAG triplet repeat in exon 1 of the gene coding for huntingtin (htt), a 348-kD soluble globular protein. htt's normal function has not yet been identified for certain. It is known to be essential for embryonic development and seems to play important roles in various cellular processes, including vesicular trafficking and coordinating intracellular signaling pathways (Harjes and Wanker, 2003; Cattaneo et al., 2005; Caviston and Holzbaur, 2009). The pathology is not simply the consequence of a loss of htt function. Instead, the expanded polyglutamine (poly-Q) tract in the N-terminal region of mutant htt (mhtt) is thought to cause in addition a toxic gain of function (Ross, 2002; Landles and Bates, 2004). Toxicity likely results from aggregated poly-Q–containing proteolytic fragments of mhtt and their interaction with other cellular proteins (Ross, 2002; Shao and Diamond, 2007; Trushina and McMurray, 2007; Imarisio et al., 2008). The actual pathomechanism is still unresolved. Particularly sensitive to mhtt are medium spiny neurons in the striatum, but other brain regions and peripheral tissues are also affected (Moffitt et al., 2009; Sassone et al., 2009). Until now, it is unclear why certain cell types are more vulnerable to mhtt-mediated toxicity than others, despite a ubiquitous expression of the htt protein both in the central nervous system and in peripheral tissues (Strong et al., 1993; Sharp et al., 1995; Trottier et al., 1995; Luthi-Carter et al., 2002; Sassone et al., 2009). The largest tissue outside the central nervous system that shows clear alterations in the disease is skeletal muscle. Weakness and wasting of muscle have been reported both in patients and in animal models of HD (Djoussé et al., 2002; Hamilton et al., 2004; Gizatullina et al., 2006; Kosinski et al., 2007; Turner et al., 2007; Busse et al., 2008). Functional measurements in living muscle fibers are only available for the R6/2 mouse model and demonstrated alterations in membrane properties and excitability (Ribchester et al., 2004). R6/2 was originally generated by Mangiarini et al. (1996) as a transgenic mouse expressing

P. Braubach, M. Orynbayev, and Z. Andronache contributed equally to this paper.

Correspondence to Werner Melzer: werner.melzer@uni-ulm.de

Abbreviations used in this paper: AM, acetomethyl; AP, action potential; DHPR, dihydropyridine receptor; Di-8-ANEPPS, di-8-amino-naphthylethenylpyridinium; ECC, excitation–contraction coupling; FDB, flexor digitorum brevis; HD, Huntington's disease; htt, huntingtin; mhtt, mutant htt; MyHC, myosin heavy chain; MyLC, myosin light chain; TTX, tetrodotoxin.

The Rockefeller University Press $30.00
J. Gen. Physiol. Vol. 144 No. 5 393–413
www.jgp.org/cgi/doi/10.1085/jgp.201411255

exon 1 of human htt containing a long (144 repeats) expanded glutamine sequence and has since then most frequently been used as a model of early onset HD.

In HD neurons, alterations in Ca^{2+} signaling have been described and suggested to be part of the pathomechanism (Tang et al., 2003, 2004, 2005, 2009; Zeron et al., 2004; Bezprozvanny, 2007, 2011; Fan and Raymond, 2007; Fernandes et al., 2007; Heng et al., 2009; Perry et al., 2010). Recently, Chen et al. (2011) found that dantrolene, a skeletal muscle relaxant, acts as a neuroprotective agent in a transgenic mouse model of HD (YAC128). Dantrolene decreases excitation-activated Ca^{2+} release from the SR in skeletal muscle (Szentesi et al., 2001; Krause et al., 2004) and is clinically important because it is the only effective antidote against malignant hyperthermia, a serious hypermetabolic complication in general anesthesia (Rosenberg et al., 2007). Malignant hyperthermia susceptibility generally results from mutations in the RyR1, the predominant Ca^{2+} release channel of the SR. The findings of Chen et al. (2011) and Suzuki et al. (2012) suggest that RyRs are involved in the pathomechanism of HD. Because RyR-based Ca^{2+} signaling is central for muscle function (Lanner et al., 2010), it may contribute to dysfunctional Ca^{2+} turnover in skeletal muscle pathology in HD. The goal of the present study was to test the hypothesis that the voltage-controlled Ca^{2+} signaling process is changed in skeletal muscle of the R6/2 mouse model of HD.

MATERIALS AND METHODS

Experimental animals and muscle fiber preparation

R6/2 mice (B6CBA-Tg (HDexon1)62Gpb/1J x C57BL6J/CBA/caF1; The Jackson Laboratory) and age-matched WT littermates were used for our experiments. The animals were bred in the specific pathogen-free facility of the Animal Research Center of Ulm University. Animal handling was in agreement with the regulations of the local animal welfare committee. Male mice were used at an age of 11–14 wk and killed by CO_2 application and rapid cervical dislocation. Interosseus muscles were dissected from the hind limb paw in Ringer's solution. Single muscle fibers were enzymatically dissociated in Ringer's solution containing 2 mg/ml collagenase, following published protocols (Liu et al., 1997; Ursu et al., 2005).

Experimental setup

Fluorescence measurements were performed using two different setups equipped with inverted microscopes (Axiovert 100 and 135 TV; Carl Zeiss). For extracellular stimulation experiments, cells were transferred to culture dishes with a coverslip bottom (MatTek Corporation) coated with Matrigel containing DMEM-F12 culture medium and equilibrated with 5% CO_2 at 37°C. After 30 min and successful fiber attachment, 2 ml of fresh culture medium was added. Fibers were kept in primary culture until measurements were performed (within 2 d after fiber preparation). Fibers were imaged with an oil-immersion objective (40×/1.30; Fluar; Carl Zeiss). Fibers eligible for analysis had to be morphologically intact and adherent to the coverslip, showing cross striation and no "blebbing" or vacuoles. Rectangular current pulses were applied by a digital-to-analogue converter (DigiData 1200; Axon Instruments) interfaced with a custom-built current booster and passed through two stainless steel electrodes immersed in the bath solution. The stimulation electrodes were positioned just outside the field of observation. Pulse duration was 0.5 ms throughout. Fluorescence was excited by a xenon light source (short arc lamp XBO 75W/2 OFR mounted in a lamp housing LH 150 with quartz condenser; Polytec) with stabilized power supply (LPS 200 X; Photo Technology International). Irradiation was controlled with an electromagnetic shutter (Uniblitz VS 25 and Shutter driver D 122; Vincent Associates) and permitted only during the recording interval to minimize photo bleaching. Emitted fluorescence was separated from the exciting light with a dichroic mirror and passed through the emission filter to a photomultiplier (PM; R 268; Hamamatsu Photonics). The recorded field was limited using an adjustable rectangular aperture (View Finder; TILL Photonics). PM signals were filtered with an eight-pole Bessel low pass filter (KF 9006; Zeitz Instrumente). Filtering and signal acquisition varied with the fluorescent probes used in the experiments. Shutter and stimulus control and fluorescence recording were performed with Clampex 8.2 software (Axon Instruments). Bath temperature was recorded with a digital thermometer (Qtemp 600; Merck Eurolab) and maintained between 25 and 26°C during the measurements. For voltage-clamp experiments, bath temperature was 20–23°C, and optical recording procedures differed only in minor details (Ursu et al., 2005).

Experimental solutions (concentrations in millimolar)

Ringer's solution for extracellular stimulation experiments contained: 145 NaCl, 5 KCl, 3.5 $MgCl_2$, 10 HEPES, and 10 glucose, pH 7.4. The external (bathing) solution for voltage-clamp experiments contained: 135 tetraethylammonium hydroxide, 135 HCH_3SO_3, 2 $MgCl_2$, 10 $CaCl_2$, 5 4-aminopyridine, 10 HEPES, 0.001 tetrodotoxin (TTX), 5 glucose, and 0.05 *N*-benzyl-*p*-toluene sulphonamide (BTS), pH 7.4. The internal (pipette) solution for intracellular dialysis contained: 145 CsOH, 135 aspartic acid, 0.75 Na_2ATP, 4.25 MgATP, 15 EGTA, 1.5 $CaCl_2$, 10 HEPES, 0.2 fura-2, and 5 sodium creatine phosphate, pH 7.2.

Action potential (AP) recording

The potentiometric fluorescent indicator dye di-8-amino-naphthylethenylpyridinium (Di-8-ANEPPS) was used to measure muscle fiber APs. The lipophilic dye accumulates in the sarcolemma and the T-tubular system. The loading protocol was adapted from Prosser et al. (2010). Fibers were subjected to 10 µM Di-8-ANEPPS in culture medium for 30 min at 37°C. APs were measured immediately after washing with the experimental Ringer's solution. For fluorescence measurements, we used an excitation filter (BP 470/20), a dichroic beam splitter (FT 493), and an emission filter (BP 505–530; all from Carl Zeiss). The signal from the PM was analogue filtered at 50 kHz and sampled at 100 kHz. A short screening protocol with four sequential pulses of different voltage (+6, −7, +8, and −9 V) was used to check cells in the dish for the presence of APs. The AP threshold was then determined with pairs of rectangular pulses of equal amplitude but opposite polarity spaced 50 ms apart. The amplitude was gradually increased from 1 to 10 V, with a 1-V increment per sweep. The AP trigger voltage was then individually set to a supra-maximal value (1 V above threshold). Pulses were applied at 1 Hz. For analysis, 20 consecutive all-or-none APs were averaged offline and smoothed by cubic spline interpolation. Averaged and smoothed signals were baseline corrected and normalized to the peak of the signal. AP recordings were used for kinetic analysis. A comparison of absolute amplitudes could not be performed because the basal background fluorescence showed considerable fiber-to-fiber variation (probably mainly resulting from dye in the Matrigel coating used for plating the cells).

Ca^{2+} recording in AP-stimulated fibers

Cells were loaded with 5 µM fura-2 in its acetomethyl (AM) ester form in Ringer's solution for 45 min. Remaining fura-2-AM was washed out with the experimental solution, and the cells were incubated for 30 min to allow for full intracellular cleavage of the acetoxymethyl ester. 100 µM of the low molecular weight myosin II blocker BTS was added to the Ringer's solution to suppress muscle contraction. During measurements, fluorescence was excited consecutively with UV light at 360 nm (near isosbestic wavelength) and 380 nm (bandwidth of 10 and 15 nm, respectively). Fibers were stimulated during the 380-nm irradiation interval. Filters were obtained from Andover Corporation and Carl Zeiss. The excitation filters were mounted in a custom-built filter changer controlled by the recording software. Fluorescence emission (intensities "F360" and "F380") was recorded at 510 nm. PM signals were analogue filtered at 5 kHz and sampled at 10 kHz. The ratio R = F380/F360 was calculated to normalize for differences in cell diameter and intracellular indicator concentration. In figures, the inverted ratio (-R) is plotted to present rising Ca^{2+} concentrations as upward-going signals. Ratios for Ca^{2+}-free (R_{min}) and Ca^{2+}-saturated (R_{max}) conditions were 3.5 and 0.7, respectively, based on calibrations as described previously (Ursu et al., 2005).

After screening for Ca^{2+} signals using a four-pulse protocol (see previous paragraph), a double-pulse paradigm (see Fig. 2 A) was applied to determine the AP threshold. Pulses of equal amplitude but opposite sign, spaced 500 ms apart, were applied. The amplitude was gradually raised from 1 to 10 V, with an increment of 1 V per sweep. The stimulation threshold was defined as the voltage that produced equal all-or-none reactions to both the positive and the negative stimulus. The pulse voltage for further measurements was set to 1 V above excitation threshold, individually for each cell.

Ca^{2+} recording in voltage-clamped fibers

Fibers were voltage clamped using a two-electrode system (Axoclamp 2B; Axon Instruments). The experiments were performed in external solution, which was designed to suppress all major ionic currents and enhance the L-type Ca^{2+} current. As described above, fluorescence emission was recorded at 510 nm during 360-nm (isosbestic) and 380-nm excitation. The experimental design, data acquisition, and experimental protocols applied were as described previously (Ursu et al., 2005; Andronache et al., 2009). R_{min} and R_{max} of fura-2 for this setup were 3.5 and 0.4, respectively. In one series of experiments, using the low affinity indicator fura-FF-AM, both intracellular electrodes were high resistance micropipettes filled with 3 M KCl. In most experiments, only the voltage recording electrode was a sharp KCl-filled micropipette. The current-passing electrode was a micropipette as used in whole-cell patch-clamp studies, which permitted intracellular dialysis with an artificial solution (see above). The high concentration of EGTA in the pipette solution suppressed contraction and generated suitable conditions for the quantification of Ca^{2+} release flux in the muscle fibers (Ursu et al., 2005).

Removal model analysis

To determine Ca^{2+} removal properties during AP-induced activation, we used a repetitive pulse protocol: A 1-s baseline measurement without stimulation was followed by a single pulse, a silent period of 500 ms, and four consecutive 50-Hz tetani, lasting 120 ms each, separated by 150-ms breaks (see Fig. 3). This protocol contains five long relaxation intervals at different levels of released Ca^{2+} and therefore intracellular binding site saturation. The relaxation time courses can be used to characterize Ca^{2+} removal (Schuhmeier and Melzer, 2004; Ursu et al., 2005). Traces were smoothed by averaging six consecutive measurements and applying an adaptive digital filter (Schuhmeier et al., 2003). A Ca^{2+} removal model that calculated binding and transport was used to simultaneously fit the time course in the long relaxation intervals. Binding to Ca^{2+}-specific (T) sites and Ca^{2+}-Mg^{2+} (P) sites of troponin C was calculated as described previously (Robertson et al., 1981; Baylor and Hollingworth, 2003). The fixed rate constant values used for the calculations at the given temperature were as follows: for T sites: $k_{on,T,Ca}$ = 115 $\mu M^{-1}s^{-1}$ and $k_{off,T,Ca}$ = 230 s^{-1}; for P sites: $k_{on,P,Ca}$ = 300 $\mu M^{-1}s^{-1}$, $k_{off,P,Ca}$ = 0.6 s^{-1}, $k_{on,P,Mg}$ = 0.1 $\mu M^{-1}s^{-1}$, and $k_{off,P,Mg}$ = 2 s^{-1}. $[T]_{tot}$ and $[P]_{tot}$, the total concentrations of T and P sites, were 240 µM each. $[Fura]_{tot}$ was 100 µM, $k_{on,Fura}$ = 180 $\mu M^{-1}s^{-1}$, and $k_{off,Fura}$ = 50 s^{-1}. Fast Ca^{2+} binding to ATP was described by a component proportional to free Ca^{2+} (scaling factor F = 3.6; Baylor and Hollingworth, 2003). In addition, a second saturable (S) and an irreversible nonsaturating binding component (NS) were included in the model to simulate any slow Ca^{2+} removal not described by the slow troponin sites (probably mainly SERCA transport to the SR, but possibly also other protein binding or transport, for instance to mitochondria). These model components were described by total concentration $[S]_{tot}$, on- and off-rate constants $k_{on,S}$ and $k_{off,S}$ (for S sites), and rate constant k_{NS} (for the NS component), respectively. These four parameters were adjusted by iteration to minimize the sum of squared deviations between calculated and measured fluorescence ratio in the relaxation phases (see Melzer et al., 1986, Schuhmeier and Melzer, 2004, and Fig. 3).

A similar repetitive pulse protocol (see Fig. 8) was used in voltage-clamp experiments on fibers dialyzed with high EGTA internal solution. In these experiments, fiber-intrinsic Ca^{2+}-binding sites could be neglected in the model simulations. The model components consisted of the indicator dye described by R_{min}; R_{max}; rate constants $k_{on,Fura}$, $k_{off,Fura}$, and concentration $[Fura]_{total}$, of a saturating buffer representing mainly EGTA (parameters $k_{on,S}$, $k_{off,S}$, and $[S]_{total}$); and an irreversible uptake mechanism (rate constant k_{NS}). $[Fura]_{total}$, $[S]_{total}$, and $K_{Fura} = k_{off,Fura}/k_{on,Fura}$ were set to fixed values of 0.2 mM, 15 mM, and 276 nM, respectively. The parameters $k_{off,Fura}$, $k_{on,S}$, $k_{off,S}$, and k_{NS} were determined by least squares fitting as described above (Ursu et al., 2005).

Ca^{2+} release calculation and Ca^{2+} current analysis

The fluorescence recordings during depolarizing pulses and the best-fit values of kinetic constants in the removal model (see above) were used to calculate the depolarization-induced Ca^{2+} flux into the myoplasmic water space, which is essentially identical to the Ca^{2+} release flux from the SR (Ursu et al., 2005). Note that the flux calculation in the voltage-clamp experiments was performed under the assumption of complete intracellular dialysis with the pipette solution. According to a previous estimate (Ursu et al., 2005), resulting amplitudes have to be scaled down by a factor of ~0.4 to take into account the incomplete cellular equilibration within the loading times of our experiments.

L-type Ca^{2+} inward current was measured in parallel with the optical signals and analyzed as described previously (Ursu et al., 2005). In brief, the voltage dependence of the leak-corrected inward current density was fitted using the term $g_{Ca,max}(V - V_{Ca})/(1 + \exp((V_{1/2} - V)/k))$, where V is the membrane potential; $g_{Ca,max}$ is the maximal Ca^{2+} conductance at large depolarizations, normalized by the linear capacitance; V_{Ca} is the apparent Ca^{2+} reversal potential; $V_{1/2}$ is the voltage of half-maximal activation; and k determines the voltage sensitivity of activation. Similarly, the voltage dependence of the Ca^{2+} input flux (peak and plateau) was fitted by the product of a single Boltzmann function ($1/(1 + \exp((V_{1/2} - V)/k))$) and a linear term (a + bV, with constants a and b).

Protein analysis

After dissection, interosseus muscles were stored at −80°C in Krebs-Ringer's solution containing 50% glycerol. For myosin heavy chain (MyHC) analysis, muscles were subjected to a protein extraction according to Singh et al. (2009). For myosin light chain

(MyLC) analysis, we used the myosin extraction procedure by Svensson et al. (1997). Protein concentration was determined using the Bradford method. Separation of proteins by SDS-PAGE was performed using a Mini-Gel system (Bio-Rad Laboratories) with 8 and 12% gels for MyHC and MyLC, respectively. The gels were stained with Roti-Blue (Carl Roth) containing the dye CBBG-250, and stained gels were scanned and analyzed using the software ImageJ (National Institutes of Health).

For quantitative Western blot analysis, muscle lysates were separated by SDS-PAGE and transferred to a PVDF membrane (Bio-Rad Laboratories) by standard procedures. Membranes were blocked in TBS-T (Tris-buffered saline with 0.1% Tween-20) containing 5% (wt/vol) nonfat dry milk for at least 1 h. After blocking, membranes were incubated with the following primary antibodies: myosin fast (1:1,000; M4276; Sigma-Aldrich), mouse anti-MyHC I (1:40; supernatant of mouse hybridoma cell line BA-F8; DSMZ), mouse anti-MyHC IIa (1:20 dilution of supernatant of mouse hybridoma cell line SC-71; DSMZ), anti-MyHC IIb (1:40; isolated from supernatant of mouse hybridoma cell line BF-F3; DSMZ), and rabbit anti-RyR1 polyclonal antibody (1:1,000; AB9078; EMD Millipore). Membranes were incubated at 4°C overnight under slow agitation. Primary antibodies were diluted in blocking solution. After three to five washing steps in TBS, membranes were incubated at room temperature for 1 h with the secondary antibody (goat anti–mouse IgG (H+L)-HPR; 1:2,500; Bio-Rad Laboratories) and Peroxidase-AffiniPure Goat Anti-Rabbit IgG (H+L) (1:10,000; Jackson ImmunoResearch Laboratories, Inc.) and washed again. Bands were visualized (ECL-immunodetection) using ImageQuant LAS 4000 (GE Healthcare). Samples were corrected for background and quantified using ImageQuant LAS 4000 software. All values were normalized to total protein amount of the corresponding lane detected by Pierce Reversible Protein Stain kits (24580; Thermo Fisher Scientific).

Software and statistics

Removal model analysis was performed using software written in Delphi (Borland) and Excel (Microsoft) macro routines (Schuhmeier and Melzer, 2004; Ursu et al., 2005). Further analysis and statistical calculations were performed using R 2.15 (R Development Core Team, 2013) running under Ubuntu Linux 12.10. Boxplots in the figures are comprised of median (line), interquartile range (IQR; box), and whiskers extending to the most extreme values within 1.5 times IQR above and below the box boundary. Data in the text are presented as mean value ± SEM (n = number of values). Group means were compared by t test, Wilcoxon test, and linear mixed effect models, treating genotype as fixed and mouse (individual) as random effect. Differences were considered significant when p-values were <0.05. Models were fitted with the lmer function provided in the R package lme4, and p-values were estimated by Markov chain Monte Carlo resampling with the pvals.fnc function of the R package languageR. In the figures and tables, significance levels are indicated as follows: *, $P < 0.05$; **, $P < 0.01$; and ***, $P < 0.001$.

RESULTS

Optical recording of APs

All physiological measurements were performed using enzymatically isolated short muscle fibers of the musculi interossei. R6/2 fibers had a significantly reduced diameter compared with WT: 36.57 ± 0.24 µm (n = 1,511) versus 46.32 ± 0.29 µm (n = 1,549; $P < 0.01$). Fiber length was not significantly different: 518.2 ± 1.8 µm (n = 1,549) in WT and 537.2 ± 2.6 µm (n = 1,511) in R6/2. However,

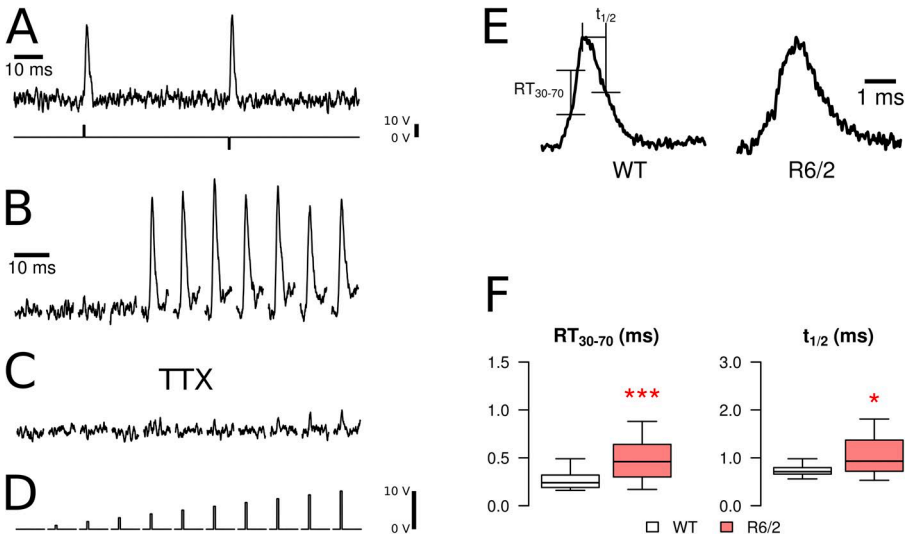

Figure 1. Fluorometric recording of APs. APs were induced in isolated fibers by extracellular electrical stimulation and recorded with the fluorescent indicator Di-8-ANEPPS. (A) A screening protocol was used containing double pulses of opposite polarity (second row). (B) All-or-none response observed when gradually increasing the pulse voltage in 1-V increments (threshold in this example: 5 V). (C) Same cell and pulse protocol as in B after the addition of 100 nM TTX to the bath solution. (D) Trigger voltages for the recordings in B and C. Recordings in A–C were from WT fibers. (E) Examples of APs (WT and R6/2, normalized) and indication of parameters to quantify kinetic changes: (a) rise time ($RT_{30–70}$) from 30 to 70% of the peak and (b) half-time of decay ($t_{1/2}$). (F) Statistical comparison of $RT_{30–70}$ and $t_{1/2}$ in fibers of WT and R6/2 mice. R6/2 fibers showed a statistically significant increase in both parameters. Data are presented as boxplots showing median (center line), interquartile range (IQR, box), and extreme values within 1.5 times IQR extending from the box limits. *, $P < 0.05$; ***, $P < 0.001$.

there was a small group (~1%) of unusually long fibers (longer than 900 μm) found in R6/2 only.

To determine temporal characteristics of APs triggered by extracellular stimulation, we used the voltage-sensitive fluorescent indicator dye Di-8-ANEPPS. Typical signals (in arbitrary units) are shown in Fig. 1 (A, B, and E). The stimulation protocol contained two pulses of equal amplitude but opposite polarity separated by a 50-ms interval (Fig. 1 A). The recordings consisted of a rapid signal, representing the AP, often followed by a more variable slow transient (see in Fig. 1 B), presumably resulting from movement. Both signals vanished when applying the sodium channel blocker TTX (100 nM). When screening cells for the presence of regenerative APs, the stimulation voltage was gradually increased using 1-V increments (Fig. 1 D). In the example shown in Fig. 1 B, the threshold for excitation was reached at 5 V. The signal showed all-or-none behavior as its super-threshold amplitude was independent of the stimulus size. The fraction of cells responding in this way was lower in R6/2 than in WT, but we did not quantify the difference because of the bias caused by the loss of fibers during isolation and plating. In TTX, only very small and short fluorescence changes persisted increasing in size with stimulation voltage (Fig. 1 C, rightmost traces). They were the result of local electrotonic responses.

AP timing parameters were compared in 21 R6/2 fibers (five mice) and 39 control fibers (five mice). Representative examples of each genotype and the statistical evaluation of kinetic parameters are shown in Fig. 1 (E and F, respectively). The rise time of the AP, from 30 to 70% of the peak ($RT_{30–70}$) of the fast fluorescence transient, was significantly longer in R6/2 compared with controls (0.49 vs. 0.29 ms; see Table 1), as was the half-time of relaxation (1.10 vs. 0.75). These data indicate certain alterations in the excitation properties despite the all-or-none behavior.

AP-induced Ca^{2+} signals

In further experiments, a similar stimulation paradigm was applied to measure intracellular Ca^{2+} signals using the indicator dye fura-2-AM (Fig. 2 A). Here, the time interval between the two pulses was 500 ms. Fig. 2 (B and C) shows a representative series of recordings from a WT fiber with increasing pulse amplitude before and after the application of 100 nM TTX, respectively. Fig. 2 B demonstrates the all-or-none behavior. After the application of TTX, the transients were blocked (Fig. 2 C). Any remaining small Ca^{2+} release was caused by local depolarizations and showed gradual increase in amplitude with increasing stimulus strength (Fig. 2 C, rightmost traces).

Representative Ca^{2+} transients of each genotype and the evaluation of their properties are shown in Fig. 2 (E and F, respectively). The AP-induced fluorescence ratio signals obtained from 101 fibers of seven R6/2 mice showed a 20% smaller mean amplitude ($-\Delta R_{peak}$) at the first pulse compared with controls (138 fibers of eight

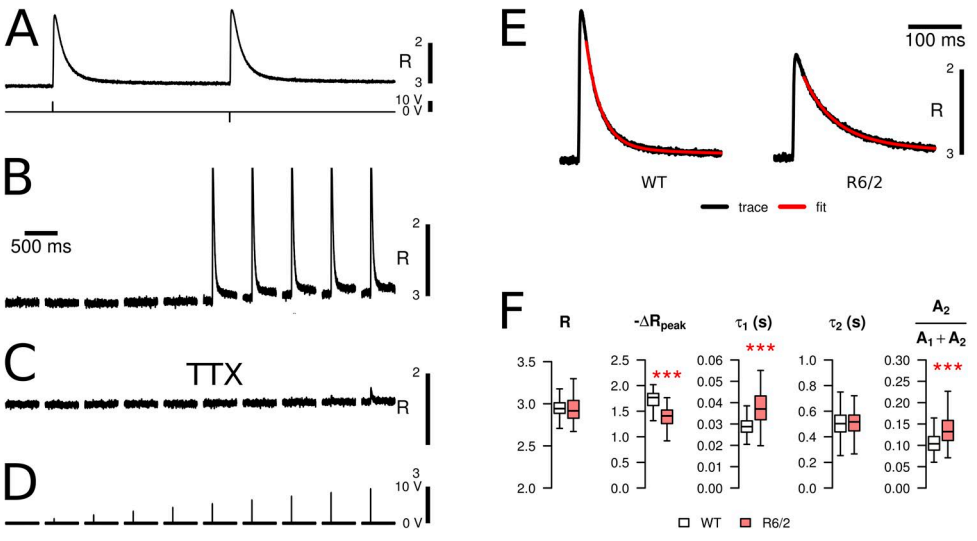

Figure 2. Calcium signals induced by APs. (A) Fura-2 calcium transients induced in an interosseus muscle fiber by extracellular electrical stimulation using a double-pulse screening protocol similar to the one in Fig. 1 A. (B) All-or-none response observed when gradually increasing the pulse voltage in 1-V increments. After reaching a threshold (here, 6 V), cells responded with a uniform signal independently of the applied voltage, resulting from the all-or-none APs. (C) Same cell and pulse protocol as in B after the addition of 100 nM TTX to the bath solution. (D) Trigger voltages for the recordings in B and C. Recordings A–C were from WT fibers. (E) Examples of fura-2 fluorescence ratio signals triggered by single super-threshold pulses in a WT and a R6/2 muscle fiber. The relaxation phases were fitted with double-exponential decay functions (red traces). (F) Statistical evaluation of signal parameters. When compared with WT controls, the R6/2 fibers showed no significant difference in the baseline fluorescence ratio (R) but a significant reduction of the signal peak ($-\Delta R_{peak}$). The relaxation time course was slower in R6/2 resulting from a significantly larger value of the smaller time constant (τ_1) and a larger relative amplitude of the slow phase (A2/(A1 + A2)). The time constant of the slow relaxation phase (τ_2) was not significantly changed. Note that this and the subsequent figures show inverted plots of the ratio signals because the fluorescence measured at 380-nm excitation decreases when the Ca^{2+} concentration rises (see Materials and methods). Data are presented as boxplots showing median (center line), interquartile range (IQR, box), and extreme values within 1.5 times IQR extending from the box limits. ***, $P < 0.001$.

TABLE 1

Parameters determined in AP stimulation experiments

Parameter	WT	R6/2	Significance
		APs	
$RT_{30–70}$ (ms)	0.286 ± 0.022	0.49 ± 0.049	***
t_{peak} (ms)	1.183 ± 0.045	1.678 ± 0.091	***
$t_{1/2}$ (ms)	0.745 ± 0.022	1.10 ± 0.112	*
		Calcium signals	
R	2.95 ± 0.008	2.938 ± 0.013	
$-\Delta R_{peak}$	1.711 ± 0.016	1.376 ± 0.022	***
τ_1 (ms)	29.69 ± 0.49	38.66 ± 0.98	***
τ_2 (ms)	512 ± 11.0	544 ± 16.9	
$A_2/(A_1 + A_2)$	0.111 ± 0.003	0.144 ± 0.005	***
		Calcium removal	
S_{tot} (mM)	2.16 ± 0.077	2.06 ± 0.601	
$k_{on,S}$ ($\mu M^{-1}s^{-1}$)	5.12 ± 0.118	11.0 ± 3.10	
$k_{off,S}$ (s^{-1})	0.733 ± 0.017	1.64 ± 0.67	
k_{NS} (s^{-1})	9,620 ± 282	4,860 ± 216	***
		Calcium release flux	
Amplitude (Ms^{-1})	0.207 ± 0.006	0.081 ± 0.003	***
t_{peak} (ms)	1.98 ± 0.041	2.75 ± 0.078	***

Parameters obtained from recordings of APs and Ca^{2+} transients elicited by extracellular stimulation. See Materials and methods and Results for definitions. Numbers of experiments (WT vs. R6/2) were 39 versus 21 for AP recordings, 138 versus 101 for Ca^{2+} transients, and 116 versus 64 for Ca^{2+} removal and Ca^{2+} release flux determination. *, $P < 0.05$; ***, $P < 0.001$.

mice; see Table 1). The difference was statistically significant ($P < 0.001$). In contrast, the mean values of the resting ratios (R) determined in a 300-ms interval of the baseline before the first stimulus were not significantly different (Table 1).

We also compared the kinetic properties of the intracellular Ca^{2+} signals by determining the time to the peak (t_{peak}) and by fitting dual-exponential functions to the decay after the peak (indicated by red lines in Fig. 2 E). The data show that the decay is slower in R6/2 fibers, resulting from increases in both the time constant τ_1 of the fast exponential and the relative contribution of the slow exponential component A_2 to the total amplitude (Fig. 2 F). The means of both increased by 30% (Table 1). The larger time constant τ_2 was unaffected. Further, we checked whether the increased time constant τ_1 was correlated with the decrease in calcium transient amplitude. In WT fibers, there was only a weak correlation (correlation coefficient $r = -0.325$ and $P = 0.0003$). R6/2 fibers showed a clearer correlation ($r = -0.717$ and $P < 0.0001$). A possible interpretation is that a common underlying mechanism is affecting both Ca^{2+} release and removal (see Discussion), and that R6/2 muscle contains a broad spectrum of differently affected fibers (from strongly altered to almost normal).

Removal model analysis of AP-induced Ca^{2+} signals

To obtain more specific information about functional changes underlying the altered amplitude and time course, we used a model that simulates the distribution of released calcium to various Ca^{2+} removal components and fitted it to measured fluorescence signals, as originally described by Melzer et al. (1986) (see also Materials and methods). To apply the removal model, isolated fibers were subjected to a paradigm (Fig. 3 C) in which a single AP was followed by four sequential trains of APs at a stimulation frequency of 50 Hz (for a similar approach

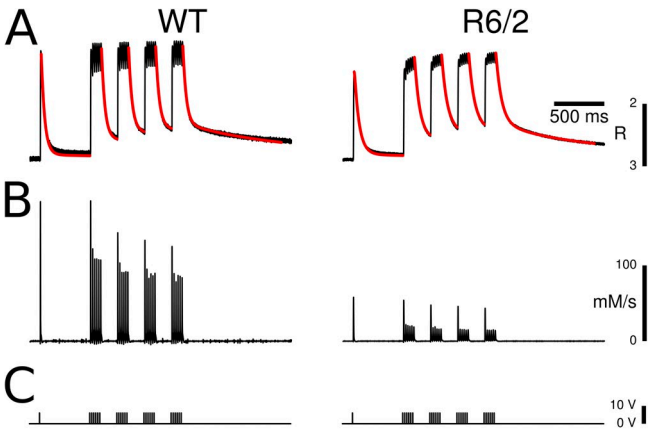

Figure 3. Removal model analysis and Ca^{2+} release flux determination. (A) A Ca^{2+} binding and transport model simulating the time course of Ca^{2+} distribution to different cellular components (see Materials and methods) was fitted simultaneously to the five long relaxation phases of fura-2 fluorescence ratio transients, which were triggered by repetitive pulsing. Red traces show the best fit to the data of the model-generated functions. (B) Ca^{2+} release flux, calculated using the best-fit model parameters. A substantial reduction of flux amplitude was found in R6/2 fibers compared with WT controls. (C) Stimulation protocol consisting of a single pulse and four 50-Hz pulse episodes.

see also Prosser et al., 2010). The first train started 500 ms after the leading pulse, and each pulse sequence was separated from the next by a 150-ms interval.

The analysis procedure provides a simultaneous best fit to all long relaxation phases of the fluorescence ratio signals by optimizing a subset of the model parameters (see Materials and methods). The model consisted of fixed components describing the binding of Ca^{2+} to the indicator dye, to troponin C, and to ATP (Robertson et al., 1981; Baylor and Hollingworth, 2003). Any residual deviation from the measured relaxation time course not described by the fixed model components was minimized by adjusting two further slow Ca^{2+} removal components: (1) a nonsaturable component (NS) exhibiting a rate proportional to free Ca^{2+} concentration, and (2) a saturable component (S) providing a second slow reversible binding compartment in addition to the Ca^{2+}-Mg^{2+} sites of troponin C. Free parameters in the model that were determined by least-squares fitting were the three rate constants (k_{NS}, $k_{on,S}$, and $k_{off,S}$) and the concentration of the saturable sites (S_{tot}). As shown in the representative examples of Fig. 3 A, the Ca^{2+} removal model provided decent fits, i.e., described well the time course of the relaxation phases both in WT and in R6/2 fibers.

Fig. 3 A demonstrates changes in the time course of the Ca^{2+} transients. A slowing in the calcium transient of the R6/2 fiber is obvious, visible in particular at the end of the last pulse train. The consequence of the slower kinetics in R6/2 fibers is a staircase-like buildup of amplitudes during the tetani that is not so evident in the WT. Consistent with the changes in the fluorescence ratio amplitude in the previously described set of measurements (Fig. 2 F), the calculated peak free Ca^{2+} concentration (after kinetic deconvolution by the model) was significantly smaller (factor 0.45). The values were 4.64 ± 0.134 µM for WT and 2.09 ± 0.065 µM for R6/2 ($P < 0.001$). The baseline free Ca^{2+} concentration was not significantly different (66.97 ± 1.19 nM for WT and 74.96 ± 2.86 nM for R6/2; $P = 0.192$). The mean values of the free removal parameters S_{tot}, $k_{on,S}$, $k_{off,S}$, and k_{NS} are listed in Table 1. Of the four parameters, k_{NS} was the only one that differed significantly (decrease to 50% of

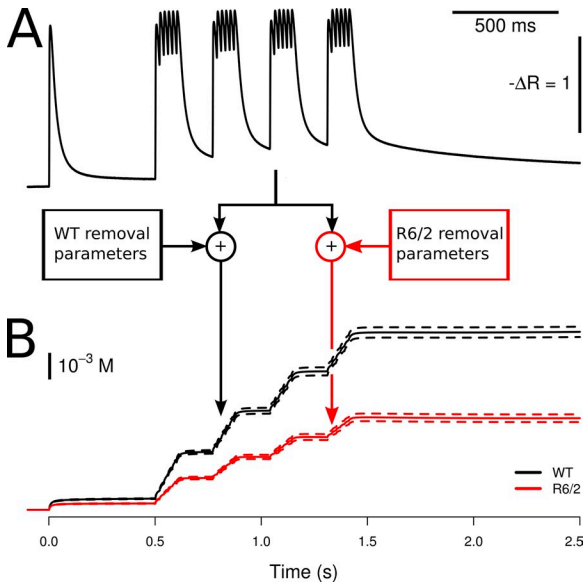

Figure 4. Lower efficiency of Ca^{2+} removal in R6/2 muscle fibers. (A) Mean WT fluorescence ratio signal (average of 120 WT measurements obtained with the protocol of Fig. 3). (B) This trace was used as a standard input signal to calculate the occupancy of the slow removal components of the model for all best-fit parameter sets obtained in the removal analysis of WT (black trace) and R6/2 measurements (red trace). The result shows a highly significant decrease in overall slow removal activity for R6/2 muscle fibers. Dashed lines indicate SEM.

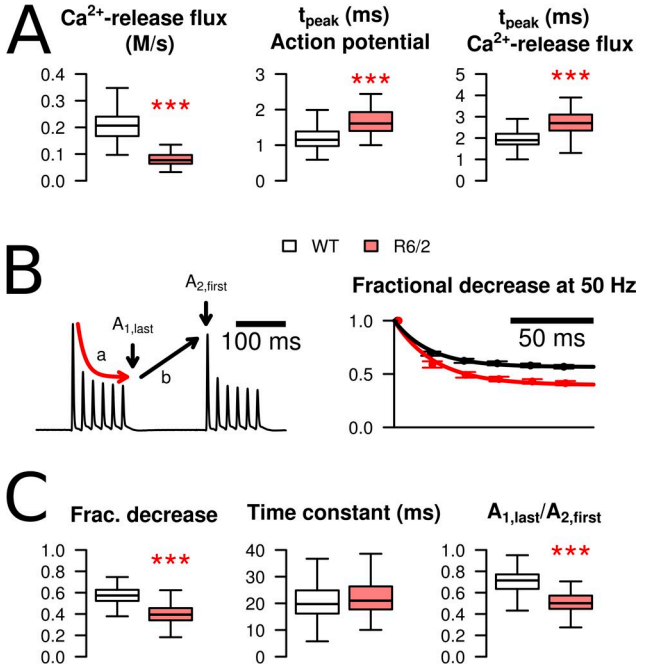

Figure 5. Characteristics of AP-triggered Ca^{2+} release flux in WT and R6/2 fibers. (A) Peak calcium release flux was significantly reduced in R6/2 (left). The time-to-peak for release flux was delayed by ~1 ms (right), paralleling a similar change in the time-to-peak of the AP (middle). (B; left) The progressive decrease of peak Ca^{2+} release flux during repetitive excitation (a) was analyzed by fitting a single-exponential decay function to the peak values of the first tetanus in the sequence. Recovery within the 150-ms interval in between tetani (b) was quantified by determining the last peak of the first tetanus ($A_{1,last}$) as a fraction of the first peak of the second tetanus ($A_{2,first}$). (Right) During the tetanus, peak Ca^{2+} release flux decreased to a lower end level in R6/2 (red trace) compared with WT fibers (black trace). (C) Statistical evaluation of decay and recovery. Fractional decrease was 0.566 ± 0.009 ($n = 116$) in WT compared with 0.397 ± 0.011 ($n = 64$) in R6/2 (***, $P < 0.001$). The time constant of the decline (middle) was not significantly different: 21 ± 1 ms in WT and 24 ± 1 ms in R6/2 ($P = 0.121$). Recovery within 150 ms was larger in R6/2 fibers, corresponding to a lower $A_{1,last}/A_{2,first}$ ratio (right): The mean ratio was 0.704 ± 0.011 in WT and 0.5 ± 0.011 in R6/2 (***, $P < 0.001$). Data in B are means ± SEM. For explanation of boxplots in A and B, see Materials and methods.

the WT value). It determines the final removal of Ca^{2+} from the cytoplasmic binding sites and seems to be the main determinant of the slower relaxation time course in R6/2 fibers.

Fig. 4 illustrates the consequences of the observed changes for overall slow removal calculated as the total amount of Ca^{2+} bound and transported by the following components: P sites of TnC, NS, and S (for definition see Materials and methods). A single fluorescence transient (arbitrarily chosen as the average of all WT measurements) was used as input, and the calculation was performed by applying all WT (Fig. 4, left) and R6/2 (right) removal parameters, respectively. It is evident that the overall clearance efficiency is greatly reduced in R6/2 fibers (red trace) compared with WT fibers (black trace). The Ca^{2+} in the three slow compartments, 500 ms after a single AP, was 57% of the WT value. 500 ms after the last tetanus, it was 52% of the corresponding WT value.

AP-induced Ca^{2+} release flux

The result of the model analysis not only provides information on Ca^{2+} removal properties, but it also leads to an estimate of the underlying Ca^{2+} release flux from the SR (Melzer et al., 1987; Ursu et al., 2005) caused by the APs. The calculated Ca^{2+} release flux derived from the fluorescence ratio traces of Fig. 3 A is shown in Fig. 3 B. On average, R6/2 fibers exhibited a considerably smaller release flux amplitude. The mean amplitude (peak Ca^{2+} release flux) for the initial single pulse was reduced to 39% (Fig. 5 A, left, and Table 1).

When analyzing further the time course of the calculated spike-like Ca^{2+} release flux, an increase in t_{peak} from 1.98 ms in WT to 2.75 ms in R6/2 was noticed (Fig. 5 A, right, Table 1). This change likely results from a corresponding change in the t_{peak} values of the APs (Fig. 5 A, middle), whose means increased from 1.18 to 1.68 ms (Table 1). The delay between AP peak and Ca^{2+} release peak can be explained by the time required for the voltage sensing by the dihydropyridine receptors (DHPRs) and the gating of the RyRs.

Within each of the four consecutive 120-ms lasting trains of stimuli (elicited at a frequency of 50 Hz), the peak Ca^{2+} release flux rapidly declined to an approximately steady level (Fig. 3 B). The decline likely results from both Ca^{2+} depletion in the SR and Ca^{2+}-dependent inactivation of the RyRs. The relative degree of Ca^{2+} release flux inhibition was significantly higher in R6/2 fibers, as shown in Fig. 5 (B and C). The mean steady level (relative to the initial peak) obtained from single-exponential least-square fits was 70% of the WT value (Fig. 5 C, left) with little change in the mean time constant of decay (Fig. 5 C, middle). The fractional recovery in the 150-ms intervals between tetani was larger in R6/2 compared with WT (Fig. 5 C, right). As a consequence, the fractional decrease of the initial peaks within the series of four tetani was not different.

Voltage clamp–induced Ca^{2+} signals

The AP-stimulated Ca^{2+} signals indicated a significant decrease in both Ca^{2+} removal activity and Ca^{2+} release flux from the SR. Because changes in APs were also detected, the specific aim of the following experiments was to determine whether the differences between R6/2 and WT muscle fibers were independent of any differences in membrane voltage. For this purpose, we controlled the muscle fiber membrane potential using a two-electrode voltage-clamp technique and studied Ca^{2+} signals elicited by voltage steps from preset holding potentials. In a first series of voltage-clamp experiments, we used sharp microelectrodes to minimize changes in the physiological properties of the intracellular space. Again, we applied the indicator dye in its AM ester form from the extracellular

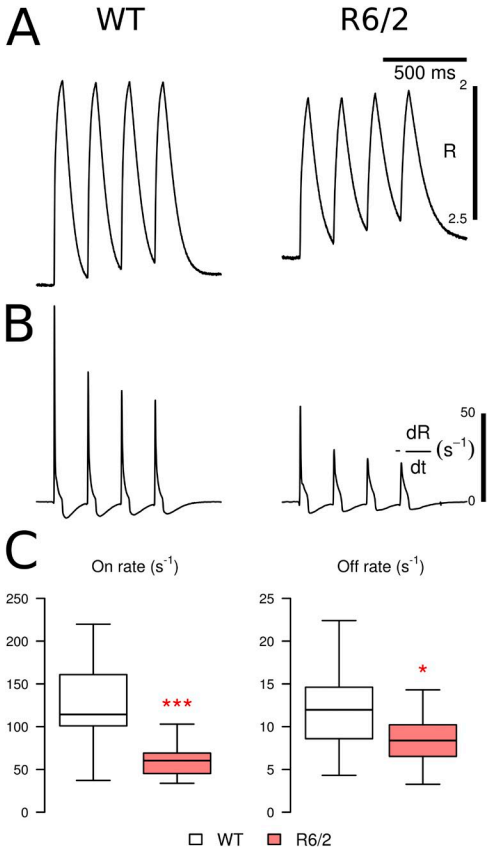

Figure 6. Evidence for reduced Ca^{2+} release and removal rates in voltage-clamped R6/2 muscle fibers. (A) Mean fura-FF fluorescence ratio signals during stimulation by four sequential 50-ms pulses to 0 mV in WT and R6/2 (18 and 11 fibers, respectively). (B) Mean time derivatives of the same sets of fibers. (C) Comparison of the maximal rates of rise (left) and decay (right) of the signals. Both mean on- and off-rates were significantly smaller in R6/2 fibers, suggesting reduced Ca^{2+} release and removal rates. Data are presented as boxplots showing median (center line), interquartile range (IQR, box), and extreme values within 1.5 times IQR extending from the box limits. *, $P < 0.05$; ***, $P < 0.001$.

space. The extracellular solution was designed to block excessive ionic currents to avoid space-clamp problems. The high affinity indicator fura-2 was chosen in the previous experiments because resting calcium and the small slow component of relaxation could be well resolved. A drawback is its nonlinearity and the necessity of a kinetic deconvolution of the ratio signals in the model analysis. Therefore, we also tried the lower affinity ratiometric Ca^{2+} indicator fura-FF (Ursu et al., 2005). However, because of the lower signal-to-noise ratio, we could not reliably evaluate removal and release kinetics by fitting model-generated curves to the individual recordings. To detect possible changes in Ca^{2+} release and removal rate in fura-FF experiments, we evaluated the maxima and minima of the time derivative during the rising and falling phase of the Ca^{2+} transients, respectively.

Fig. 6 shows results obtained with a repetitive activation protocol similar to the one used in Fig. 3: a sequence of four 50-ms voltage steps to 0 mV was applied, separated by intervals of 150 ms. The figure shows the mean fluorescence ratio signal (Fig. 6 A) and the corresponding mean time derivative (Fig. 6 B) obtained from 18 WT fibers and 11 R6/2 fibers (five and six mice, respectively). Both the peak rate of rise at the onset of the pulse and the peak rate of decrease at the end of the pulse were significantly smaller in the R6/2 group (Fig. 6 C). Moreover, the R6/2 group contained three fibers (not included in the analysis of Fig. 6 C), which differed from the rest of the cells by their much slower decay time course. No fiber with comparable characteristics was found among the WT group in this series of measurements. Therefore, consistent with the results from AP-triggered Ca^{2+} signals, these findings in voltage-clamped fibers likewise point to reduced effectiveness in removing released Ca^{2+} from the cytoplasmic space and to a considerable decrease in Ca^{2+} release flux.

Ca^{2+} release determination in voltage-clamped muscle fibers

Next, we used a method that facilitates the calculation of Ca^{2+} release flux in voltage-clamped fibers. In these experiments, the current-passing electrode was exchanged for a patch pipette–like low resistance microelectrode that allowed us to dialyze the intracellular space with an isosmolar artificial solution. The pipette solution contained a high concentration (15 mM) of EGTA and fura-2 (200 µM). These conditions simplify the model description of cytoplasmic Ca^{2+} binding because released Ca^{2+} is predominantly bound to EGTA (González and Ríos, 1993; Schuhmeier et al., 2003; Schuhmeier and Melzer, 2004; Ursu et al., 2005). In addition, the artificial internal solution prevents movement, buffers intracellular ATP, and contains Cs^+ to eliminate residual K^+ outward currents. This permitted the recording of L-type Ca^{2+} currents originating from the DHPR ($Ca_V1.1$) in parallel to the Ca^{2+} transients, which we found not feasible in nondialyzed fibers because of substantial ionic current contamination. Fig. 7 shows

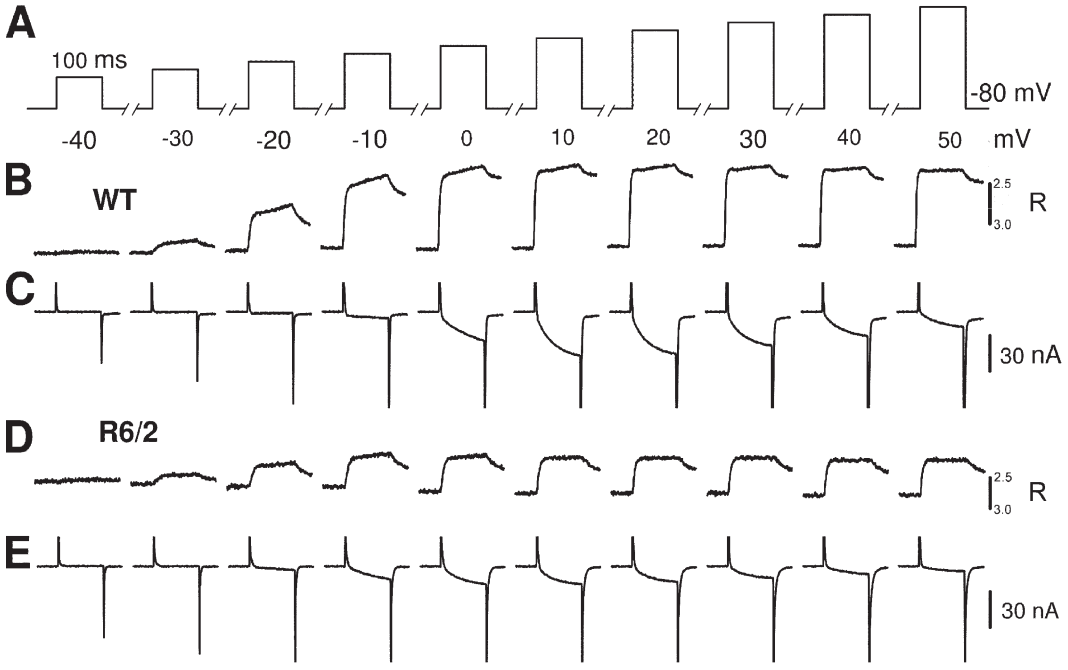

Figure 7. Activation of L-type Ca^{2+} currents and fluorometric Ca^{2+} transients by step depolarizations to different voltages in dialyzed muscle fibers. (A) Rectangular voltage pulses of 100-ms duration and different amplitude. (B and D) Changes in fura-2 fluorescence ratio R in muscle fibers of a WT and a R6/2 mouse, respectively. (C and E) L-type Ca^{2+} currents recorded simultaneously in the same fibers. Note that the rapid phases at the beginning and end of the recordings are partly truncated. Linear capacitance values of the two fibers were 4.60 nF for WT and 2.17 nF for R6/2.

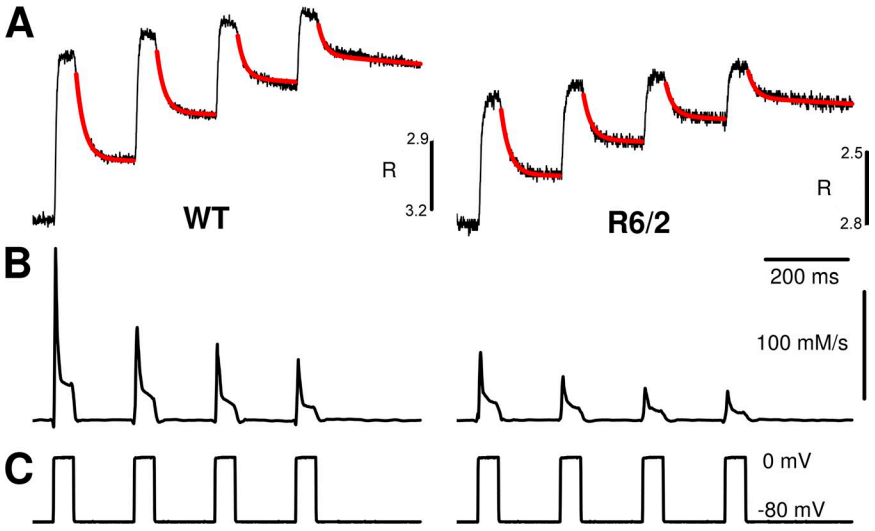

Figure 8. Model fit to determine Ca^{2+} removal and Ca^{2+} release. (A) Representative fura-2 fluorescence ratio traces obtained during repetitive pulse activation in a WT and a R6/2 muscle fiber. The kinetic model described in Materials and methods with free parameters $k_{off,Fura}$, $k_{on,S}$, $k_{off,S}$, and k_{NS} was used to generate the curves highlighted in red and to fit them to the measured data. Mean best-fit parameter values are listed in Table 2. (B) Ca^{2+} release flux calculated using the best-fit parameters of A. (C) Changes in membrane voltage that elicited the signals in A.

examples of recordings of simultaneously measured Ca^{2+} currents (C and E) and Ca^{2+} transients (B and D) for different step voltages between −40 and +50 mV. The time course of the Ca^{2+} transients is determined by the strong EGTA buffering and the kinetics of fura-2 (Struk et al., 1998). At pulse off, an elevated, very slowly decaying component (truncated in Fig. 7) is discernable, resulting from the dissociation of Ca^{2+} that was bound to EGTA during the pulse and the slow rate of Ca^{2+} return to the SR.

To determine the time course of the Ca^{2+} release flux in these experiments, we performed a removal model fit comparable to that used in the analysis of AP-triggered Ca^{2+} signals. The procedure profits from the fact

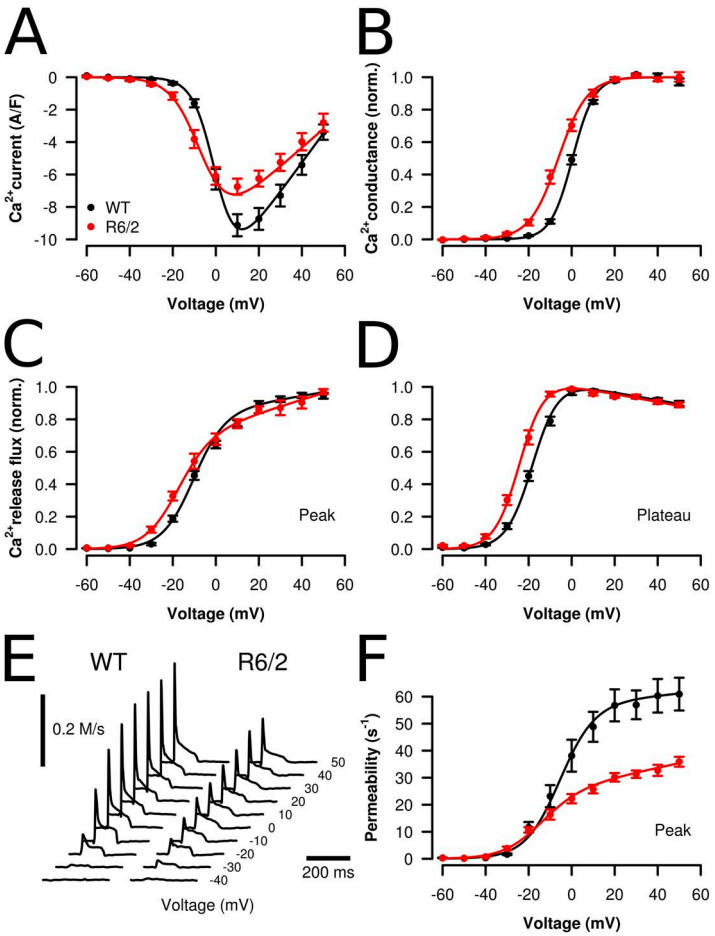

Figure 9. Voltage dependence of Ca^{2+} entry and release signals in muscle fibers from WT and R6/2 mice. (A) Voltage dependence of L-type Ca^{2+} current density. (B) Normalized Ca^{2+} conductance derived from the data shown in A. Black symbols and lines (n = 17), WT; red symbols and lines (n = 9), R6/2. (C) Normalized peak Ca^{2+} release flux. (D) Normalized plateau of Ca^{2+} release flux, determined as the average of the values between 25 and 75 ms after pulse-on. Values from the different experiments were averaged after normalization to the maximum (WT, n = 19; R6/2, n = 10). (E) Representative Ca^{2+} release flux traces at different pulse voltages of a WT and a R6/2 fiber. (F) Peak SR Ca^{2+} permeability (in s^{-1}, corresponding to 0.1%/ms) derived from the Ca^{2+} release flux traces evaluated in C and D. For parameter comparison, see Table 2. The curves were generated using the parameter mean values. Data are means ± SEM.

that the high intracellular EGTA is the dominating Ca^{2+} buffer in the cytoplasm (for details see Schuhmeier et al., 2003, Schuhmeier and Melzer, 2004, and Ursu et al., 2005). Representative examples of the model fit (red traces) to fura-2 ratio signals and the calculated Ca^{2+} release flux are shown in Fig. 8 (A and B, respectively).

Voltage dependence of Ca^{2+} entry and release gating

Fig. 9 presents analysis results for the voltage-dependent activation of both Ca^{2+} current and Ca^{2+} signals. Fig. 9 A indicates two differences in the L-type Ca^{2+} current of R6/2 fibers: a decrease in maximal amplitude and a lower threshold for activation. Fig. 9 B demonstrates the threshold change in the voltage gating of the channels: Plotting the fractional activation of normalized L-type conductance as a function of the membrane potential shows a significant shift of ~7 mV to more negative membrane potentials in the R6/2 fibers. The absolute value of maximal conductance per fiber capacitance was decreased by 35% from 180 S/F in WT to 117 S/F in R6/2 (Table 2). The decrease in L-type channel conductance was accompanied by a similar (30%) decrease in the amplitude of the fluorescence ratio signal at maximal activation and a lower threshold of voltage-dependent Ca^{2+} release activation. $V_{1/2}$ differed by 8 mV. The plots of Fig. 9 (C and D) demonstrate the voltage threshold change in R6/2 fibers for the peak and the plateau phase of the Ca^{2+} release flux, respectively. In another series of experiments with nondialyzed fibers, in which Ca^{2+} current data were not available, amplitude was likewise reduced, but no significant voltage shift could be noticed.

TABLE 2

Parameters determined in voltage-clamp experiments

Parameter	WT	R6/2	Significance
L-type calcium current			
Activation			
$V_{1/2}$ (mV)	0.40 ± 0.56	−6.20 ± 1.14	***
k (mV)	5.05 ± 0.18	6.68 ± 0.46	***
g_{max} (SF^{-1})	180 ± 9.06	117 ± 10.59	***
V_{rev} (mV)	69.21 ± 2.38	77.33 ± 5.83	
C_m (nF)	5.26 ± 0.40	3.64 ± 0.48	*
Availability			
$V_{1/2}$ (mV)	−31.03 ± 1.24	−30.20 ± 1.43	
k (mV)	8.32 ± 0.42	9.32 ± 0.50	
Calcium removal			
$k_{off,Fura}$ (s^{-1})	39.90 ± 2.48	40.73 ± 3.89	
$k_{on,S}$ ($\mu M^{-1}s^{-1}$)	26.71 ± 3.62	48.41 ± 16.81	
$k_{off,S}$ (s^{-1})	6.11 ± 0.76	5.11 ± 1.01	
k_{NS} (s^{-1})	7,743 ± 1,256	8,114 ± 2,718	
Calcium release flux (peak)			
Activation			
$V_{1/2}$ (mV)	−10.81 ± 1.43	−18.71 ± 0.80	***
k (mV)	7.29 ± 0.39	7.76 ± 0.33	
a ($Ms^{-1}V^{-1}$)	1.11 ± 0.43	0.53 ± 0.15	
b (Ms^{-1})	0.245 ± 0.034	0.092 ± 0.017	***
Max (Ms^{-1})	0.293 ± 0.047	0.119 ± 0.021	**
Availability			
$V_{1/2}$ (mV)	−37.95 ± 0.10	−42.51 ± 1.18	*
k (mV)	5.68 ± 0.42	4.89 ± 0.26	
Calcium release permeability (peak)			
Activation			
$V_{1/2}$ (mV)	−5.81 ± 1.99	−15.82 ± 2.31	**
k (mV)	8.08 ± 0.48	9.10 ± 0.79	
a ($s^{-1}mV^{-1}$)	0.077 ± 0.095	0.169 ± 0.033	
b (s^{-1})	57.37 ± 5.94	26.97 ± 1.42	***
Max (s^{-1})	60.92 ± 6.06	35.90 ± 1.83	***

Best-fit parameters describing voltage dependence of activation and steady-state availability of L-type Ca^{2+} current and Ca^{2+} release and of the removal model used for calculating Ca^{2+} release flux. Numbers of experiments (WT vs. R6/2) were 17 versus 9 for L-type Ca^{2+} current activation and 20 versus 11 for availability, 19 versus 10 for Ca^{2+} removal fit and Ca^{2+} release activation, and 18 versus 11 for Ca^{2+} release availability. V_{rev}, reversal potential; C_m, linear capacitance; Max, maximal value at +50 mV. For definitions of the other parameters, see Materials and methods. *, $P < 0.05$; **, $P < 0.01$; ***, $P < 0.001$.

Qualitatively, the phasic time course of the traces (Figs. 8 B and 9 E) resembles the response to repetitive stimulation by APs (Fig. 3 B). However, the fractional decline in flux amplitude was generally smaller during a spike sequence compared with equally long voltage steps, possibly caused by the lower effective depolarization and lower fractional SR depletion during a series of short spikes. It is generally assumed that the rapid decline after the peak results from both inactivation of RyRs and SR depletion, whereas the subsequent slow decline reflects mainly depletion during a residual steady RyR activity. Using this assumption, we subjected the Ca^{2+} release flux traces to a correction for the putative depletion effect to derive an estimate of the voltage-activated changes in SR Ca^{2+} permeability (Schneider et al., 1987; González and Ríos, 1993). The voltage dependence of peak permeability is shown in Fig. 9 F (parameters are listed in Table 2). The amplitude at maximal depolarization to +50 mV (Max) decreased to 59% of the WT value (Table 2). This procedure also provides an estimate of the initial Ca^{2+} content of the release compartment (concentration relative to myoplasmic water space). The values (in millimolar for the +50-mV steps) were 5.14 ± 0.61 for WT and 3.40 ± 0.51 for R6/2 ($P < 0.05$), assuming full loading of the cell with the pipette solution. Using the approximate estimate of 0.4 of mean fractional fiber dialysis at the time of the measurements (Ursu et al., 2005), the estimated values are 2.06 and 1.36 mM, respectively.

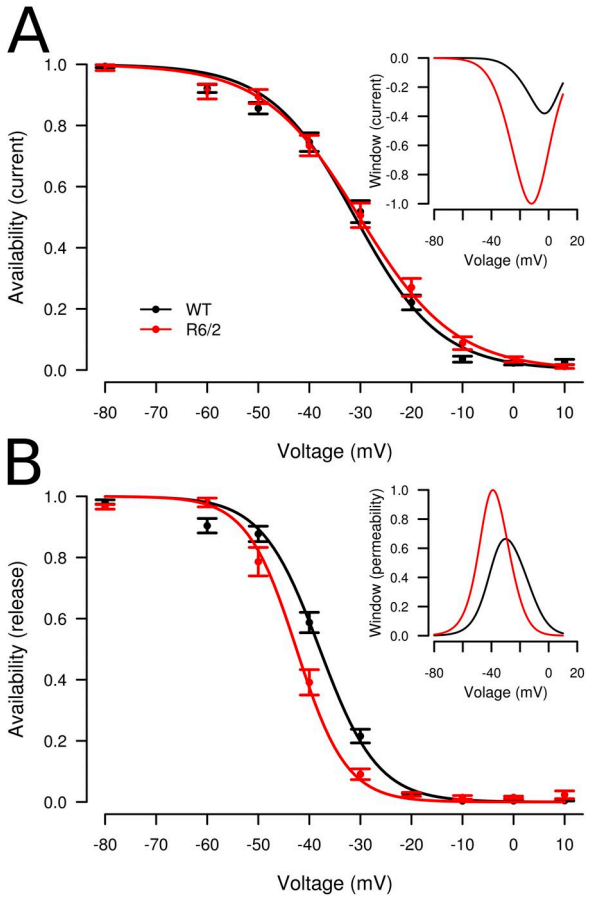

Figure 10. Voltage-dependent availability of Ca^{2+} current and Ca^{2+} release. (A) Fractional availability of L-type Ca^{2+} current in WT (black; $n = 20$) and R6/2 (red; $n = 11$) muscle fibers. Data of each fiber were fitted by canonical Boltzmann functions. (B) Fractional availability of peak Ca^{2+} flux in WT ($n = 18$) and R6/2 ($n = 11$) muscle fibers. For the best-fit parameters, see Table 2. The curves were constructed using the mean values of $V_{1/2}$ and k (see Table 2). The insets show relative steady-state window current and window permeability calculated by multiplying each voltage dependence of availability by the voltage dependence of inward current (Fig. 9 A) and permeability (plateau after the peak), respectively. The maximum values for R6/2 (red traces) were used for normalizing the window curves. These values were 0.384 A/F (current) and 0.183 s^{-1} (permeability), respectively. Data are means ± SEM.

Both L-type Ca^{2+} current and Ca^{2+} release flux exhibit a slow voltage-dependent inactivation when depolarization is maintained over seconds (for references see Melzer, 2013). We performed further experiments to investigate whether a change in steady-state inactivation might have caused the decrease in maximal Ca^{2+} signal activation. We applied an inactivation protocol using progressively decreasing levels of polarization (for intervals of 30 s each), followed by a test step of 100 ms to +20 mV. The response to the test pulse decreases with conditioning voltage (Fig. 10). Fits of the voltage dependence using canonical Boltzmann functions showed no significant differences for Ca^{2+} current, but a shift in $V_{1/2}$ to the left by 4.6 mV for Ca^{2+} release (Table 2). This relatively small change could hardly explain the dramatic decrease in SR Ca^{2+} permeability shown in Fig. 9 F and might be a consequence of the shift in activation resulting in a change in the voltage dependence of steady-state SR depletion (see Melzer, 2013, and Robin and Allard, 2013). The insets show estimates of the relative size of steady-state Ca^{2+} current (Fig. 10 A) and Ca^{2+} permeability (Fig. 10 B) for the same range of potentials determined by combining the voltage dependence of availability and activation (see Fig. 10 legend and Discussion).

Myosin isotype determination and RyR1 quantification

Previous results on human HD and mouse R6/2 muscle showing changes in the mRNA expression patterns (Strand et al., 2005) and fiber histology (Ribchester et al., 2004) suggested a transition to slower fiber-type characteristics. It has been reported that slow fibers of the mouse soleus muscle release Ca^{2+} at a much lower rate per AP than fast fibers of the extensor digitorum longus muscle (Baylor and Hollingworth, 2003, 2012). Therefore, it could be suspected that the functional changes observed by us result from a fast to slow transition in fiber type. A frequently used method to distinguish slow (type I) from fast (type II) muscle is determining the various myosin isoforms (Pette and Staron, 1997; Steinacker et al., 2000; Toniolo et al., 2007; Friedrich et al., 2008;

Schiaffino and Reggiani, 2011). To test whether changes in myosin isoforms are detectable in R6/2 interosseus muscles, we performed SDS gel electrophoresis of muscle extracts using published protocols (Svensson et al., 1997; Singh et al., 2009). Both MyHCs and MyLCs were separated using gels of different density (see Fig. 11, A–C, and Materials and methods). As reported previously by Friedrich et al. (2008), the interosseus is a type IIA muscle (fast, oxidative). In our electrophoresis experiments, we confirmed this finding (Fig. 11, A–C), but we also noticed a small band of type I (~10%) and traces of type IIx MyHCs (<1%). Comparing the relative amounts of I and IIa heavy chains in WT and R6/2 muscles showed no significant alteration (Fig. 11 C, left). Changes, even if only small, were confined to the light chain pattern (Fig. 11 C, right). These results rule out that our functional observations originate from fiber-type transformations.

Finally, to check whether the dramatic decrease in Ca^{2+} release activity that we found results from a lower density of release channels, we quantified RyR1 protein expression by Western blotting using specific antibodies. Fig. 11 D shows representative blots (top) and Fig. 11 E shows the evaluation of all measurements as the RyR1 stain normalized to the total protein stain. The differences between WT and R6/2 interosseus were not significant. These results, therefore, indicate that the decrease in Ca^{2+} release is not caused by a reduced RyR1 expression.

DISCUSSION

Calcium pathology in HD and skeletal muscle effects

htt, which in its mutant form (mhtt) is the cause of the neurodegenerative pathology of HD, is widely expressed in neuronal cells but is equally abundant in other tissues (Strong et al., 1993; Sharp et al., 1995; Trottier et al., 1995; Luthi-Carter et al., 2002; Sassone et al., 2009). Several studies indicated that abnormal neuronal Ca^{2+}

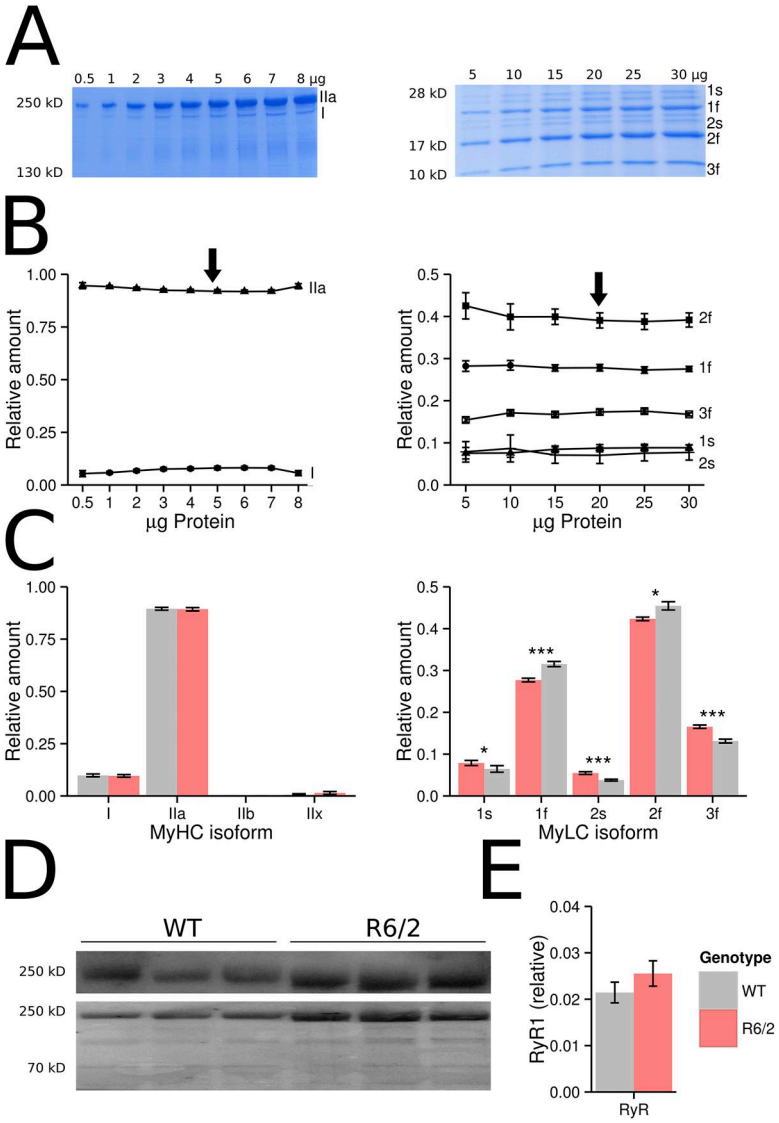

Figure 11. Quantification of myosin and RyR1. (A–C) SDS gel electrophoretic separation of MyHCs and MyLCs and (D and E) quantitative Western blot analysis of RyR1. (A) Representative gels (WT) stained with Roti-Blue. Different concentrations of protein were loaded on 8% (MyHC) and 12% (MyLC) gels. (B) Mean fractional contributions of the different isoforms (left, MyHC; right, MyLC; n = 10 experiments, respectively, of the sort shown in A). 5 µg of protein extract was used for the comparative MyHC quantification, and 20 µg of the myosin extract was used for MyLC quantification (arrows). (C) Comparison of fractional contribution of the MyHC (left) and MyLC (right) isoforms in WT and R6/2 interosseus. Because results for male and female mice were almost identical, they were pooled for the graphics. (D) Western blots of RyR1 from WT and R6/2 interosseus, and for each lane the corresponding total protein stain. (E) RyR1 (relative to stained protein) shows no significant difference between WT (0.021 ± 0.002; n = 12) and R6/2 (0.0272 ± 0.002; n = 12) interosseus. Data are means ± SEM. *, $P < 0.05$; ***, $P < 0.001$.

signaling plays a critical role in promoting neuronal death in HD (Cepeda et al., 2001; Bezprozvanny and Hayden, 2004; Tang et al., 2005, 2009; Shehadeh et al., 2006; Bezprozvanny, 2007, 2011; Fernandes et al., 2007). Recently, the muscle relaxant dantrolene and other inhibitors of RyRs have been shown to reduce neuronal cell death (Chen et al., 2011; Suzuki et al., 2012). Because skeletal muscle is one of the peripheral tissues affected in HD (Sharp et al., 1995; Orth et al., 2003; Ciammola et al., 2006; Sassone et al., 2009) and RyR1 plays a pivotal role in this tissue, our attention focused on the voltage-controlled RyR1-based Ca^{2+} signaling in skeletal muscle of the mouse HD model R6/2 (Mangiarini et al., 1996). Ca^{2+} signaling in skeletal muscle can be disturbed by alterations in (a) Ca^{2+} influx through plasma membrane channels, (b) release of Ca^{2+} from intracellular stores, (c) the membrane potential signal that controls these fluxes, and (d) Ca^{2+} removal from the cytoplasm. In this study, we demonstrated changes in all four aspects of muscular Ca^{2+} signaling.

Fiber morphology, myosin isoforms, and membrane excitation

Ribchester et al. (2004) investigated morphology and fiber membrane properties of R6/2 skeletal muscle. Electrophysiology was performed by this group on flexor digitorum brevis (FDB) muscle fibers because of their short-cable properties. We used the interosseus, a muscle that exhibits equally short fibers and, unlike FDB, consists largely of a single fiber type (fast oxidative, type IIA; Friedrich et al., 2008, and this study). In agreement with the results of Ribchester et al. (2004) and Sathasivam et al. (1999) from FDB and quadriceps of R6/2 mice, the mean diameter of a large number of evaluated interosseus fibers was 21% smaller compared with WT. According to previous investigations, the change in muscle bulk in R6/2 mice results from a uniform fiber shrinkage without any evidence of myopathy (Sathasivam et al., 1999) except for certain abnormalities in the neuromuscular junctions, possibly suggesting altered trophic interaction with the motor neurons (Ribchester et al., 2004). One hypothesis to explain alterations in HD muscle was a transition from fast to slower fiber-type characteristics (Ribchester et al., 2004; Strand et al., 2005). Slow-twitch fibers are thinner and release a third to a fourth of the amount of Ca^{2+} per AP than fast fibers and show a lower capacity to store Ca^{2+} (Baylor and Hollingworth, 2003, 2012; Trinh and Lamb, 2006; Murphy et al., 2009). Typical characteristics of a change in fiber type are alterations in the MyHCs (Pette and Staron, 1997; Steinacker et al., 2000; Toniolo et al., 2007; Friedrich et al., 2008; Schiaffino and Reggiani, 2011). In the interosseus muscle, we detected no alteration in the relative amount of MyHC isoforms. Therefore, the functional changes that we observed in this muscle do not seem to result from a prototypical fast to slow transformation in fiber type. This is in line with recent findings indicating that fiber properties including Ca^{2+} signaling may change independently of MyHC content (Calderón et al., 2010; Canepari et al., 2010; Delbono, 2010). Small but significant changes were seen by us in the light chain pattern of myosin (Fig. 11 C) and might go in parallel with adaptations in the excitation–contraction coupling (ECC) apparatus. Although we could not detect any differences in the amount of RyR1 (Fig. 11 E) between WT and R6/2 interosseus, RyR1-associated proteins may be affected and deserve attention in future studies.

In FDB fibers of symptomatic R6/2 mice, Ribchester et al. (2004) measured lower resting potentials than in WT (by ∼10 mV), a higher input resistance, and a threefold larger membrane time constant. Moreover, a substantially higher incidence of anode-break APs was seen in R6/2 fibers, which may indicate a higher degree of inactivation of the voltage-dependent sodium channels caused by the partial depolarization. In general agreement with these findings, we observed an increase in rise time and time-to-peak of 71 and 42%, respectively, and a 48% increase in the half-time of decay of optically recorded APs. The fact that APs could be completely suppressed in our experiments by 100 nM TTX argues against a significant exchange of $Na_V1.4$ for $Na_V1.5$, i.e., a variant with low TTX sensitivity (White et al., 1991), as suggested by Ribchester et al. (2004). In any case, as discussed below, our results rule out that the observed changes in fiber excitation are sufficient to explain the differences in Ca^{2+} signaling reported here.

Changes in Ca^{2+} removal

The slower kinetics of Ca^{2+} relaxation in R6/2 fibers at the end of a single AP or a train of APs indicate changes in the mechanisms that clear the myoplasm of released Ca^{2+}. We simulated Ca^{2+} binding and clearance using a kinetic model (see Materials and methods) in which the parameters of the fast and slow sites of troponin C were fixed to values obtained from the literature (Robertson et al., 1981; Baylor and Hollingworth, 2003), whereas a saturating and a nonsaturating slow transport mechanism were adjusted to fit the measured relaxation time course. In addition, we tried seven other variants of the model to test the sensitivity of the result to changes in the assumptions. These alternative analyses included (a) a decrease in the off-rate constant of the fast sites of troponin C by a factor of 10 to a value originally reported by Robertson et al. (1981), (b) the use of only a single freely adjustable slow binding component (i.e., omission of the fixed set of slow Ca^{2+}-Mg^{2+} sites of troponin C), and (c) an increase in the K_D value of fura-2 by a factor of 3 (by lowering the on-rate constant) to account for possible effects of the protein environment on the indicator dye (Konishi et al., 1988). All analyses produced qualitatively similar results, leading to a significant decrease in the extent of slow Ca^{2+} removal (as shown

in Fig. 4). A likely candidate to explain these changes is the SERCA calcium pump, the ATP-driven enzyme that is responsible for SR reloading after Ca^{2+} release. Myoplasmic buffers (like parvalbumin) or Ca^{2+} uptake by mitochondria (Weiss et al., 2010; Yi et al., 2011) could also contribute to the difference in Ca^{2+} removal. Parvalbumin is absent in type IIA fibers of mice (Füchtbauer et al., 1991), but mitochondria are highly abundant and defects in mitochondrial function have been described for R6/2 muscle (Gizatullina et al., 2006; see below).

Changes in Ca^{2+} release and Ca^{2+} inward current

A significant reduction in muscle strength measured with a handheld dynamometer has been reported in people with HD. HD patients presented about half the isometric strength of healthy matched control subjects when different muscle groups were tested (Busse et al., 2008). A possible reason is dysfunctional Ca^{2+} release. Because Ca^{2+} binding and transport is quantified in the Ca^{2+} removal analysis, summing the time derivatives of all Ca^{2+} components provides a straightforward way to estimate the total Ca^{2+} flux (input flux) into the myoplasm (Melzer et al., 1987; Timmer et al., 1998; Schuhmeier and Melzer, 2004; Ursu et al., 2005). This flux is essentially identical to Ca^{2+} release from the SR (Ursu et al., 2005). The mean amplitude of Ca^{2+} input flux of intact R6/2 fibers stimulated by APs was found to be only 39% of that in WT fibers. To exclude that the strong difference in Ca^{2+} removal activity (Fig. 4 B) determined in our model analysis simply results from smaller flux rates, we used the mean WT Ca^{2+} release flux, scaled down by the same factor, as input to the same model (same parameters) to simulate artificial fluorescence ratio traces. The analysis of the simulated ratio led to identical overall slow removal activity in contrast to the result of Fig. 4 B.

The voltage-clamp technique allowed for the study in further detail of the alterations in Ca^{2+} release and, in addition, permitted the assessment of properties of the voltage-dependent Ca^{2+} entry from the extracellular space (Ursu et al., 2005). Voltage-clamp experiments on nondialyzed R6/2 fibers (i.e., with minimally disturbed intracellular space) showed similar results as those found in AP-stimulated fibers: The maximum rate of rise and rate of decay of the fluorescence ratio signal were significantly smaller than in WT fibers, pointing to a smaller peak Ca^{2+} release flux and reduced Ca^{2+} removal activity (Fig. 6). In agreement with these findings, dialyzed R6/2 fibers also showed a significantly reduced Ca^{2+} release flux (to 41%; Table 2). The correction for putative Ca^{2+} depletion (Schneider et al., 1987; González and Ríos, 1993) indicated a significantly smaller peak SR Ca^{2+} permeability than WT fibers (to 59%). On average, the Ca^{2+} content of the SR, simultaneously estimated with this method, was reduced to 66% in R6/2 compared with WT fibers, with a relatively large fiber-to-fiber variance. Therefore, the decreased Ca^{2+} release flux in R6/2 fibers may originate from a combination of smaller Ca^{2+} permeability and (to a lesser degree) lower SR Ca^{2+} load, perhaps as a consequence of the reduced uptake activity (see Fig. 4). A less effective reuptake may also explain the stronger decrease in peak release seen in repetitively stimulated R6/2 muscle fibers (Fig. 5 B).

Voltage-activated Ca^{2+} inward current is a further potential source of cytoplasmic Ca^{2+}, and neuronal Ca^{2+} channels have been reported to be targets of htt (Miller and Bezprozvanny, 2010). In skeletal muscle, L-type Ca^{2+} channels serve as voltage sensors for RyR1 activation. Their Ca^{2+} inward current contributes much less than RyR1-mediated Ca^{2+} release to the myoplasmic Ca^{2+} elevation (Ursu et al., 2005). Although maximal L-type Ca^{2+} current was reduced in R6/2 fibers, it was actually larger than in WT, at voltages up to 0 mV, caused by its more negative threshold of activation (Fig. 9 A). Because the steady-state characteristics of voltage-dependent inactivation were unchanged (Fig. 10 A), an increase in window Ca^{2+} inward current and therefore an increase in a small but persistent Ca^{2+} flow from the extracellular space into fibers, depending on the degree of depolarization at rest (see inset in Fig. 10 A), is predicted. This effect might enhance any preexisting depolarization and cause cellular Ca^{2+} overload in partially depolarized fibers.

Potential mechanisms explaining mhtt effects on muscle ECC

Because of the highly disabling impact of muscle weakness and atrophy resulting from disuse, aging, or disease, the mechanisms of such weakness are the targets of intense research (Jackman and Kandarian, 2004; Marzetti et al., 2010; Weiss et al., 2010; Rüegg and Glass, 2011; Romanick et al., 2013). Functional changes in addition to atrophy often lead to stronger weakness than expected from the change in muscle mass alone (Manring et al., 2014). Specifically, ECC, the most prominent process in muscle that affects Ca^{2+} homeostasis, is changed in various pathologies (Rossi and Dirksen, 2006; Friedrich et al., 2008; Hollingworth et al., 2008; Teichmann et al., 2008; Andronache et al., 2009; Zhou et al., 2010; Delbono, 2011; Manring et al., 2014). Our results from R6/2 mice indicate that this is also true for skeletal muscle in HD.

Toxic poly-Q–containing proteolytic peptides of mhtt that interact with functional proteins are the basis of HD pathology (Ross, 2002; Shao and Diamond, 2007; Trushina and McMurray, 2007; Imarisio et al., 2008). The scheme in Fig. 12 provides a working hypothesis that combines our findings with the results of previous studies, demonstrating the effects of mhtt on cellular energetics and Ca^{2+} regulation (Arenas et al., 1998; Lodi et al., 2000; Panov et al., 2002; Choo et al., 2004; Gellerich et al., 2004, 2008; Saft et al., 2005; Gizatullina et al., 2006; Lin and Beal, 2006; Turner et al., 2007; Bossy-Wetzel et al., 2008; Turner and Schapira, 2010; Chen et al., 2011; Suzuki et al., 2012).

There is evidence that mhtt affects mitochondrial function early during disease development (Arenas et al., 1998; Panov et al., 2002; Milakovic and Johnson, 2005; Saft et al., 2005; Ciammola et al., 2006, 2011; Gizatullina et al., 2006; Turner et al., 2007; Bossy-Wetzel et al., 2008; Chaturvedi et al., 2009; Costa et al., 2010; Turner and Schapira, 2010; Mochel and Haller, 2011). Mitochondria are in close contact to the SR, generate ATP for SR Ca^{2+} transport, and may even directly contribute to the rapid Ca^{2+} sequestration during ECC (Boncompagni et al., 2009; Weiss et al., 2010; Yi et al., 2011; Eisner et al., 2013), probably involving the recently identified mitochondrial calcium uniporter (De Stefani et al., 2011; Patron et al., 2013). Therefore, mitochondrial impairment will inevitably affect Ca^{2+} signaling. One likely mechanism involves excess production of reactive redox radicals (Sun et al., 2001; Brookes et al., 2004; Eisner et al., 2013; Wang et al., 2013) that can modify thiol residues in RyR1 (activation) and the SERCA calcium pump (inhibition) (Favero et al., 1995; Moreau et al., 1998; Viner et al., 1999; Sun et al., 2001). Uncompensated Ca^{2+} leak, mediated by oxidized RyR1 (Suzuki et al., 2012), would lead to partial SR unloading and to a destructive feed-forward cycle (Fig. 12, blue arrows), as has been proposed for muscle expressing overactive mutant RyR1 causing malignant hyperthermia (Durham et al., 2008). In this context, it is interesting that weight loss in spite of increased caloric intake has been observed in HD and has been attributed to an early hypermetabolic state of peripheral body tissue (Mochel et al., 2007). Mitochondrial Ca^{2+} overload resulting from the rise in cytoplasmic Ca^{2+} concentration would initially enhance the cycle and finally lead to the opening of the mitochondrial permeability transition pore, resulting in the collapse of the mitochondrial membrane potential, the major driving force for mitochondrial Ca^{2+} uptake (Brookes et al., 2004; Rasola and Bernardi, 2007). Chronically increased myoplasmic Ca^{2+} concentration is known to uncouple the transverse tubules (Fig. 12, TT) from the SR by hydrolysis of the connecting protein junctophilin, probably by Ca^{2+}-dependent proteases (calpains; see Murphy et al., 2013), resulting in the inhibition of voltage-activated Ca^{2+} release (red dashed arrow), as found in our experiments.

Instead of being caused by a primary dysfunction of the energy metabolism, the events outlined in Fig. 12 could also be initiated by a direct effect of mhtt on the Ca^{2+} release units. A specific interaction between the htt-associated protein 1 and both inositol-3-phosphate receptors and RyR has been reported for the brain (Varshney and Ehrlich, 2003; Lindenberg, K.S., A. Davranche, F. Klein, A.V. Thomas, C. Lill, T. Lenk, L.R. Orlando, J. Kama, A.B. Young, G.B. Landwehrmeyer, and Y. Trottier. 2010. Sixth European Huntington's Disease Network Plenary Meeting. Abstr. A20). Similarly as reported for aged fast muscle (Damiani et al., 1996; Russ et al., 2011; but see Renganathan and Delbono, 1998), a simple reduction of cellular RyR1 content does not seem to be the cause of the strongly suppressed Ca^{2+} release that we found

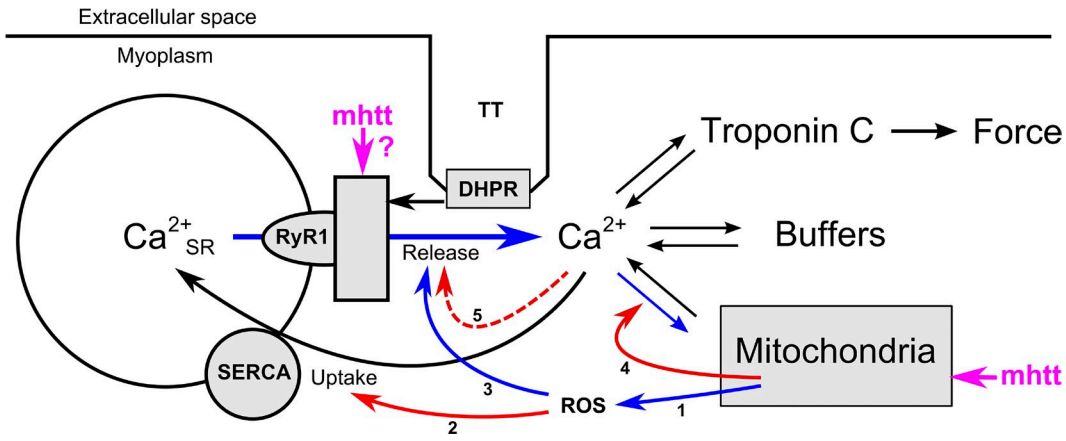

Figure 12. Hypothetical mechanism of poly-Q toxicity in skeletal muscle ECC. In skeletal muscle, the depolarization of the transverse tubular system (TT) is sensed by the DHPR ($Ca_V1.1$) and causes the release of Ca^{2+} from the terminal cisternae of the SR via RyRs (RyR1). The released Ca^{2+} ions initiate contraction by binding to troponin C. Ca^{2+} is also bound to other cytoplasmic sites (summarized as "buffers," including the indicator dye in the experimental setting). In parallel, Ca^{2+} is pumped back into the lumen of the SR by transport ATPases (SERCA) and is taken up by mitochondria. The scheme combines several documented mechanisms (see Discussion for references) that could explain the reduced Ca^{2+} release and Ca^{2+} removal in R6/2 muscle fibers identified in this study: Mitochondria, challenged by mhtt, release ROS (1) causing thiol oxidation of SR proteins. SERCA is inhibited (2), and RyR1 is activated (3) by ROS-induced oxidation. The resulting rise in the cytoplasmic Ca^{2+} concentration causes mitochondrial Ca^{2+} overload and is part of a feed-forward cycle (labeled in blue) that further enhances SR Ca^{2+} leak. Chronically elevated cytoplasmic Ca^{2+} concentration eventually uncouples TT and SR as a result of calpain-mediated hydrolysis of junctophilin (5). Uptake into mitochondria will cease (4) when the mitochondrial membrane depolarizes in response to Ca^{2+} overload. In the scheme, the continuous red arrows mark mechanisms that reduce Ca^{2+} removal from the cytoplasm, whereas the dashed red arrow marks a reduction in Ca^{2+} release that would counteract depletion of the SR. In addition to its effect on mitochondria, mhtt may also modulate RyR1 directly.

(Fig. 11 E). Measurements on isolated Ca^{2+} release channels would be important to determine whether mhtt has a direct functional effect on RyR1.

In conclusion, the results presented here provide strong evidence for severely disturbed Ca^{2+} homeostasis in R6/2 skeletal muscle. Ca^{2+} entry, Ca^{2+} release, and Ca^{2+} removal were found to be reduced. Failure in ECC may, therefore, be a major cause for muscle weakness in HD, supporting the hypothesis that RyR1 function is affected. We suspect that these changes are interlinked with the reported energetic deficits caused by mhtt. Further studies are needed to pinpoint the specific primary sites of action that lead to the observed alterations in muscular Ca^{2+} signaling.

We thank Mrs. Astrid Bellan-Koch, Mrs. Karin Fuchs, and Mr. Achim Riecker for expert technical help. We are grateful to Dr. Oliver Friedrich and Mrs. Cornelia Weber in the Medical Biophysics Group of Dr. Rainer A.H. Fink (University of Heidelberg) for teaching us the SDS-PAGE technique.

Deutsche Forschungsgemeinschaft grant ME 713/18 to W. Melzer is gratefully acknowledged.

The authors declare no competing financial interests.

Richard L. Moss served as editor.

Submitted: 9 July 2014
Accepted: 2 October 2014

REFERENCES

Andronache, Z., S.L. Hamilton, R.T. Dirksen, and W. Melzer. 2009. A retrograde signal from RyR1 alters DHP receptor inactivation and limits window Ca^{2+} release in muscle fibers of Y522S RyR1 knock-in mice. *Proc. Natl. Acad. Sci. USA.* 106:4531–4536. http://dx.doi.org/10.1073/pnas.0812661106

Arenas, J., Y. Campos, R. Ribacoba, M.A. Martín, J.C. Rubio, P. Ablanedo, and A. Cabello. 1998. Complex I defect in muscle from patients with Huntington's disease. *Ann. Neurol.* 43:397–400. http://dx.doi.org/10.1002/ana.410430321

Baylor, S.M., and S. Hollingworth. 2003. Sarcoplasmic reticulum calcium release compared in slow-twitch and fast-twitch fibres of mouse muscle. *J. Physiol.* 551:125–138. http://dx.doi.org/10.1113/jphysiol.2003.041608

Baylor, S.M., and S. Hollingworth. 2012. Intracellular calcium movements during excitation–contraction coupling in mammalian slow-twitch and fast-twitch muscle fibers. *J. Gen. Physiol.* 139:261–272. http://dx.doi.org/10.1085/jgp.201210773

Bezprozvanny, I. 2007. Inositol 1,4,5-tripshosphate receptor, calcium signalling and Huntington's disease. *Subcell. Biochem.* 45:323–335. http://dx.doi.org/10.1007/978-1-4020-6191-2_11

Bezprozvanny, I. 2011. Role of inositol 1,4,5-trisphosphate receptors in pathogenesis of Huntington's disease and spinocerebellar ataxias. *Neurochem. Res.* 36:1186–1197. http://dx.doi.org/10.1007/s11064-010-0393-y

Bezprozvanny, I., and M.R. Hayden. 2004. Deranged neuronal calcium signaling and Huntington disease. *Biochem. Biophys. Res. Commun.* 322:1310–1317. http://dx.doi.org/10.1016/j.bbrc.2004.08.035

Boncompagni, S., A.E. Rossi, M. Micaroni, S.L. Hamilton, R.T. Dirksen, C. Franzini-Armstrong, and F. Protasi. 2009. Characterization and temporal development of cores in a mouse model of malignant hyperthermia. *Proc. Natl. Acad. Sci. USA.* 106:21996–22001. http://dx.doi.org/10.1073/pnas.0911496106

Bossy-Wetzel, E., A. Petrilli, and A.B. Knott. 2008. Mutant huntingtin and mitochondrial dysfunction. *Trends Neurosci.* 31:609–616. http://dx.doi.org/10.1016/j.tins.2008.09.004

Brookes, P.S., Y. Yoon, J.L. Robotham, M.W. Anders, and S.S. Sheu. 2004. Calcium, ATP, and ROS: a mitochondrial love-hate triangle. *Am. J. Physiol. Cell Physiol.* 287:C817–C833. http://dx.doi.org/10.1152/ajpcell.00139.2004

Busse, M.E., G. Hughes, C.M. Wiles, and A.E. Rosser. 2008. Use of hand-held dynamometry in the evaluation of lower limb muscle strength in people with Huntington's disease. *J. Neurol.* 255:1534–1540. http://dx.doi.org/10.1007/s00415-008-0964-x

Calderón, J.C., P. Bolaños, and C. Caputo. 2010. Myosin heavy chain isoform composition and Ca^{2+} transients in fibres from enzymatically dissociated murine soleus and extensor digitorum longus muscles. *J. Physiol.* 588:267–279. http://dx.doi.org/10.1113/jphysiol.2009.180893

Canepari, M., M.A. Pellegrino, G. D'Antona, and R. Bottinelli. 2010. Single muscle fiber properties in aging and disuse. *Scand. J. Med. Sci. Sports.* 20:10–19. http://dx.doi.org/10.1111/j.1600-0838.2009.00965.x

Cattaneo, E., C. Zuccato, and M. Tartari. 2005. Normal huntingtin function: an alternative approach to Huntington's disease. *Nat. Rev. Neurosci.* 6:919–930. http://dx.doi.org/10.1038/nrn1806

Caviston, J.P., and E.L. Holzbaur. 2009. Huntingtin as an essential integrator of intracellular vesicular trafficking. *Trends Cell Biol.* 19:147–155. http://dx.doi.org/10.1016/j.tcb.2009.01.005

Cepeda, C., M.A. Ariano, C.R. Calvert, J. Flores-Hernández, S.H. Chandler, B.R. Leavitt, M.R. Hayden, and M.S. Levine. 2001. NMDA receptor function in mouse models of Huntington disease. *J. Neurosci. Res.* 66:525–539. http://dx.doi.org/10.1002/jnr.1244

Cepeda, C., N. Wu, V.M. André, D.M. Cummings, and M.S. Levine. 2007. The corticostriatal pathway in Huntington's disease. *Prog. Neurobiol.* 81:253–271. http://dx.doi.org/10.1016/j.pneurobio.2006.11.001

Chaturvedi, R.K., P. Adhihetty, S. Shukla, T. Hennessy, N. Calingasan, L. Yang, A. Starkov, M. Kiaei, M. Cannella, J. Sassone, et al. 2009. Impaired PGC-1α function in muscle in Huntington's disease. *Hum. Mol. Genet.* 18:3048–3065. http://dx.doi.org/10.1093/hmg/ddp243

Chen, X., J. Wu, S. Lvovskaya, E. Herndon, C. Supnet, and I. Bezprozvanny. 2011. Dantrolene is neuroprotective in Huntington's disease transgenic mouse model. *Mol. Neurodegener.* 6:81. http://dx.doi.org/10.1186/1750-1326-6-81

Choo, Y.S., G.V. Johnson, M. MacDonald, P.J. Detloff, and M. Lesort. 2004. Mutant huntingtin directly increases susceptibility of mitochondria to the calcium-induced permeability transition and cytochrome c release. *Hum. Mol. Genet.* 13:1407–1420. http://dx.doi.org/10.1093/hmg/ddh162

Ciammola, A., J. Sassone, L. Alberti, G. Meola, E. Mancinelli, M.A. Russo, F. Squitieri, and V. Silani. 2006. Increased apoptosis, Huntingtin inclusions and altered differentiation in muscle cell cultures from Huntington's disease subjects. *Cell Death Differ.* 13:2068–2078. http://dx.doi.org/10.1038/sj.cdd.4401967

Ciammola, A., J. Sassone, M. Sciacco, N.E. Mencacci, M. Ripolone, C. Bizzi, C. Colciago, M. Moggio, G. Parati, V. Silani, and G. Malfatto. 2011. Low anaerobic threshold and increased skeletal muscle lactate production in subjects with Huntington's disease. *Mov. Disord.* 26:130–137. http://dx.doi.org/10.1002/mds.23258

Costa, V., M. Giacomello, R. Hudec, R. Lopreiato, G. Ermak, D. Lim, W. Malorni, K.J. Davies, E. Carafoli, and L. Scorrano. 2010. Mitochondrial fission and cristae disruption increase the response of cell models of Huntington's disease to apoptotic stimuli. *EMBO Mol. Med.* 2:490–503. http://dx.doi.org/10.1002/emmm.201000102

Damiani, E., L. Larsson, and A. Margreth. 1996. Age-related abnormalities in regulation of the ryanodine receptor in rat fast-twitch muscle. *Cell Calcium.* 19:15–27. http://dx.doi.org/10.1016/S0143-4160(96)90010-X

De Stefani, D., A. Raffaello, E. Teardo, I. Szabò, and R. Rizzuto. 2011. A forty-kilodalton protein of the inner membrane is the mitochondrial calcium uniporter. *Nature.* 476:336–340. http://dx.doi.org/10.1038/nature10230

Delbono, O. 2010. Myosin–still a good reference for skeletal muscle fibre classification? *J. Physiol.* 588:9. http://dx.doi.org/10.1113/jphysiol.2009.184598

Delbono, O. 2011. Expression and regulation of excitation-contraction coupling proteins in aging skeletal muscle. *Curr. Aging Sci.* 4:248–259. http://dx.doi.org/10.2174/1874609811104030248

Djoussé, L., B. Knowlton, L.A. Cupples, K. Marder, I. Shoulson, and R.H. Myers. 2002. Weight loss in early stage of Huntington's disease. *Neurology.* 59:1325–1330. http://dx.doi.org/10.1212/01.WNL.0000031791.10922.CF

Durham, W.J., P. Aracena-Parks, C. Long, A.E. Rossi, S.A. Goonasekera, S. Boncompagni, D.L. Galvan, C.P. Gilman, M.R. Baker, N. Shirokova, et al. 2008. RyR1 S-nitrosylation underlies environmental heat stroke and sudden death in Y522S RyR1 knockin mice. *Cell.* 133:53–65. http://dx.doi.org/10.1016/j.cell.2008.02.042

Eisner, V., G. Csordás, and G. Hajnóczky. 2013. Interactions between sarco-endoplasmic reticulum and mitochondria in cardiac and skeletal muscle–pivotal roles in Ca^{2+} and reactive oxygen species signaling. *J. Cell Sci.* 126:2965–2978. http://dx.doi.org/10.1242/jcs.093609

Fan, M.M., and L.A. Raymond. 2007. *N*-methyl-D-aspartate (NMDA) receptor function and excitotoxicity in Huntington's disease. *Prog. Neurobiol.* 81:272–293. http://dx.doi.org/10.1016/j.pneurobio.2006.11.003

Favero, T.G., A.C. Zable, and J.J. Abramson. 1995. Hydrogen peroxide stimulates the Ca^{2+} release channel from skeletal muscle sarcoplasmic reticulum. *J. Biol. Chem.* 270:25557–25563. http://dx.doi.org/10.1074/jbc.270.43.25557

Fernandes, H.B., K.G. Baimbridge, J. Church, M.R. Hayden, and L.A. Raymond. 2007. Mitochondrial sensitivity and altered calcium handling underlie enhanced NMDA-induced apoptosis in YAC128 model of Huntington's disease. *J. Neurosci.* 27:13614–13623. http://dx.doi.org/10.1523/JNEUROSCI.3455-07.2007

Friedrich, O., C. Weber, F. von Wegner, J.S. Chamberlain, and R.H. Fink. 2008. Unloaded speed of shortening in voltage-clamped intact skeletal muscle fibers from wt, mdx, and transgenic minidystrophin mice using a novel high-speed acquisition system. *Biophys. J.* 94:4751–4765. http://dx.doi.org/10.1529/biophysj.107.126557

Füchtbauer, E.M., A.M. Rowlerson, K. Götz, G. Friedrich, K. Mabuchi, J. Gergely, and H. Jockusch. 1991. Direct correlation of parvalbumin levels with myosin isoforms and succinate dehydrogenase activity on frozen sections of rodent muscle. *J. Histochem. Cytochem.* 39:355–361. http://dx.doi.org/10.1177/39.3.1825216

Gellerich, F.N., S. Trumbeckaite, T. Müller, M. Deschauer, Y. Chen, Z. Gizatullina, and S. Zierz. 2004. Energetic depression caused by mitochondrial dysfunction. *Mol. Cell. Biochem.* 256–257:391–405. http://dx.doi.org/10.1023/B:MCBI.0000009885.34498.e6

Gellerich, F.N., Z. Gizatullina, H.P. Nguyen, S. Trumbeckaite, S. Vielhaber, E. Seppet, S. Zierz, B. Landwehrmeyer, O. Riess, S. von Hörsten, and F. Striggow. 2008. Impaired regulation of brain mitochondria by extramitochondrial Ca^{2+} in transgenic Huntington disease rats. *J. Biol. Chem.* 283:30715–30724. http://dx.doi.org/10.1074/jbc.M709555200

Gizatullina, Z.Z., K.S. Lindenberg, P. Harjes, Y. Chen, C.M. Kosinski, B.G. Landwehrmeyer, A.C. Ludolph, F. Striggow, S. Zierz, and F.N. Gellerich. 2006. Low stability of Huntington muscle mitochondria against Ca^{2+} in R6/2 mice. *Ann. Neurol.* 59:407–411. http://dx.doi.org/10.1002/ana.20754

González, A., and E. Ríos. 1993. Perchlorate enhances transmission in skeletal muscle excitation–contraction coupling. *J. Gen. Physiol.* 102:373–421. http://dx.doi.org/10.1085/jgp.102.3.373

Hamilton, J.M., T. Wolfson, G.M. Peavy, M.W. Jacobson, and J. Corey-Bloom. Huntington Study Group. 2004. Rate and correlates of weight change in Huntington's disease. *J. Neurol. Neurosurg. Psychiatry.* 75:209–212. http://dx.doi.org/10.1136/jnnp.2003.017822

Harjes, P., and E.E. Wanker. 2003. The hunt for huntingtin function: interaction partners tell many different stories. *Trends Biochem. Sci.* 28:425–433. http://dx.doi.org/10.1016/S0968-0004(03)00168-3

Heng, M.Y., P.J. Detloff, P.L. Wang, J.Z. Tsien, and R.L. Albin. 2009. In vivo evidence for NMDA receptor-mediated excitotoxicity in a murine genetic model of Huntington disease. *J. Neurosci.* 29:3200–3205. http://dx.doi.org/10.1523/JNEUROSCI.5599-08.2009

Hollingworth, S., U. Zeiger, and S.M. Baylor. 2008. Comparison of the myoplasmic calcium transient elicited by an action potential in intact fibres of mdx and normal mice. *J. Physiol.* 586:5063–5075. http://dx.doi.org/10.1113/jphysiol.2008.160507

Imarisio, S., J. Carmichael, V. Korolchuk, C.W. Chen, S. Saiki, C. Rose, G. Krishna, J.E. Davies, E. Ttofi, B.R. Underwood, and D.C. Rubinsztein. 2008. Huntington's disease: from pathology and genetics to potential therapies. *Biochem. J.* 412:191–209. http://dx.doi.org/10.1042/BJ20071619

Jackman, R.W., and S.C. Kandarian. 2004. The molecular basis of skeletal muscle atrophy. *Am. J. Physiol. Cell Physiol.* 287:C834–C843. http://dx.doi.org/10.1152/ajpcell.00579.2003

Konishi, M., A. Olson, S. Hollingworth, and S.M. Baylor. 1988. Myoplasmic binding of fura-2 investigated by steady-state fluorescence and absorbance measurements. *Biophys. J.* 54:1089–1104. http://dx.doi.org/10.1016/S0006-3495(88)83045-5

Kosinski, C.M., C. Schlangen, F.N. Gellerich, Z. Gizatullina, M. Deschauer, J. Schiefer, A.B. Young, G.B. Landwehrmeyer, K.V. Toyka, B. Sellhaus, and K.S. Lindenberg. 2007. Myopathy as a first symptom of Huntington's disease in a marathon runner. *Mov. Disord.* 22:1637–1640. http://dx.doi.org/10.1002/mds.21550

Krause, T., M.U. Gerbershagen, M. Fiege, R. Weisshorn, and F. Wappler. 2004. Dantrolene—A review of its pharmacology, therapeutic use and new developments. *Anaesthesia.* 59:364–373. http://dx.doi.org/10.1111/j.1365-2044.2004.03658.x

Landles, C., and G.P. Bates. 2004. Huntingtin and the molecular pathogenesis of Huntington's disease. Fourth in molecular medicine review series. *EMBO Rep.* 5:958–963. http://dx.doi.org/10.1038/sj.embor.7400250

Lanner, J.T., D.K. Georgiou, A.D. Joshi, and S.L. Hamilton. 2010. Ryanodine receptors: Structure, expression, molecular details, and function in calcium release. *Cold Spring Harb. Perspect. Biol.* 2:a003996. http://dx.doi.org/10.1101/cshperspect.a003996

Lin, M.T., and M.F. Beal. 2006. Mitochondrial dysfunction and oxidative stress in neurodegenerative diseases. *Nature.* 443:787–795. http://dx.doi.org/10.1038/nature05292

Liu, Y., S.L. Carroll, M.G. Klein, and M.F. Schneider. 1997. Calcium transients and calcium homeostasis in adult mouse fast-twitch skeletal muscle fibers in culture. *Am. J. Physiol.* 272:C1919–C1927.

Lodi, R., A.H. Schapira, D. Manners, P. Styles, N.W. Wood, D.J. Taylor, and T.T. Warner. 2000. Abnormal in vivo skeletal muscle energy metabolism in Huntington's disease and dentatorubropallidoluysian atrophy. *Ann. Neurol.* 48:72–76. http://onlinelibrary.wiley.com/doi/10.1002/1531-8249%28200007%2948:1%3C72::AID-ANA11%3E3.0.CO;2-I/abstract

Luthi-Carter, R., S.A. Hanson, A.D. Strand, D.A. Bergstrom, W. Chun, N.L. Peters, A.M. Woods, E.Y. Chan, C. Kooperberg, D. Krainc, et al. 2002. Dysregulation of gene expression in the R6/2

model of polyglutamine disease: parallel changes in muscle and brain. *Hum. Mol. Genet.* 11:1911–1926. http://dx.doi.org/10.1093/hmg/11.17.1911

Mangiarini, L., K. Sathasivam, M. Seller, B. Cozens, A. Harper, C. Hetherington, M. Lawton, Y. Trottier, H. Lehrach, S.W. Davies, and G.P. Bates. 1996. Exon 1 of the HD gene with an expanded CAG repeat is sufficient to cause a progressive neurological phenotype in transgenic mice. *Cell.* 87:493–506. http://dx.doi.org/10.1016/S0092-8674(00)81369-0

Manring, H., E. Abreu, L. Brotto, N. Weisleder, and M. Brotto. 2014. Novel excitation-contraction coupling related genes reveal aspects of muscle weakness beyond atrophy—new hopes for treatment of musculoskeletal diseases. *Front Physiol.* 5:37. http://dx.doi.org/10.3389/fphys.2014.00037

Marzetti, E., J.C. Hwang, H.A. Lees, S.E. Wohlgemuth, E.E. Dupont-Versteegden, C.S. Carter, R. Bernabei, and C. Leeuwenburgh. 2010. Mitochondrial death effectors: Relevance to sarcopenia and disuse muscle atrophy. *Biochim. Biophys. Acta.* 1800:235–244. http://dx.doi.org/10.1016/j.bbagen.2009.05.007

Melzer, W. 2013. Skeletal muscle fibers: Inactivated or depleted after long depolarizations? *J. Gen. Physiol.* 141:517–520. http://dx.doi.org/10.1085/jgp.201310997

Melzer, W., E. Ríos, and M.F. Schneider. 1986. The removal of myoplasmic free calcium following calcium release in frog skeletal muscle. *J. Physiol.* 372:261–292.

Melzer, W., E. Rios, and M.F. Schneider. 1987. A general procedure for determining the rate of calcium release from the sarcoplasmic reticulum in skeletal muscle fibers. *Biophys. J.* 51:849–863. http://dx.doi.org/10.1016/S0006-3495(87)83413-6

Milakovic, T., and G.V. Johnson. 2005. Mitochondrial respiration and ATP production are significantly impaired in striatal cells expressing mutant huntingtin. *J. Biol. Chem.* 280:30773–30782. http://dx.doi.org/10.1074/jbc.M504749200

Miller, B.R., and I. Bezprozvanny. 2010. Corticostriatal circuit dysfunction in Huntington's disease: intersection of glutamate, dopamine and calcium. *Future Neurol.* 5:735–756. http://dx.doi.org/10.2217/fnl.10.41

Mochel, F., and R.G. Haller. 2011. Energy deficit in Huntington disease: why it matters. *J. Clin. Invest.* 121:493–499. http://dx.doi.org/10.1172/JCI45691

Mochel, F., P. Charles, F. Seguin, J. Barritault, C. Coussieu, L. Perin, Y. Le Bouc, C. Gervais, G. Carcelain, A. Vassault, et al. 2007. Early energy deficit in Huntington disease: Identification of a plasma biomarker traceable during disease progression. *PLoS ONE.* 2:e647. http://dx.doi.org/10.1371/journal.pone.0000647

Moffitt, H., G.D. McPhail, B. Woodman, C. Hobbs, and G.P. Bates. 2009. Formation of polyglutamine inclusions in a wide range of non-CNS tissues in the HdhQ150 knock-in mouse model of Huntington's disease. *PLoS ONE.* 4:e8025. http://dx.doi.org/10.1371/journal.pone.0008025

Moreau, V.H., R.F. Castilho, S.T. Ferreira, and P.C. Carvalho-Alves. 1998. Oxidative damage to sarcoplasmic reticulum Ca^{2+}-ATPase AT submicromolar iron concentrations: evidence for metal-catalyzed oxidation. *Free Radic. Biol. Med.* 25:554–560. http://dx.doi.org/10.1016/S0891-5849(98)00084-7

Murphy, R.M., N.T. Larkins, J.P. Mollica, N.A. Beard, and G.D. Lamb. 2009. Calsequestrin content and SERCA determine normal and maximal Ca^{2+} storage levels in sarcoplasmic reticulum of fast- and slow-twitch fibres of rat. *J. Physiol.* 587:443–460. http://dx.doi.org/10.1113/jphysiol.2008.163162

Murphy, R.M., T.L. Dutka, D. Horvath, J.R. Bell, L.M. Delbridge, and G.D. Lamb. 2013. Ca^{2+}-dependent proteolysis of junctophilin-1 and junctophilin-2 in skeletal and cardiac muscle. *J. Physiol.* 591:719–729. http://dx.doi.org/10.1113/jphysiol.2012.243279

Orth, M., J.M. Cooper, G.P. Bates, and A.H. Schapira. 2003. Inclusion formation in Huntington's disease R6/2 mouse muscle cultures. *J. Neurochem.* 87:1–6. http://dx.doi.org/10.1046/j.1471-4159.2003.02009.x

Panov, A.V., C.A. Gutekunst, B.R. Leavitt, M.R. Hayden, J.R. Burke, W.J. Strittmatter, and J.T. Greenamyre. 2002. Early mitochondrial calcium defects in Huntington's disease are a direct effect of polyglutamines. *Nat. Neurosci.* 5:731–736.

Patron, M., A. Raffaello, V. Granatiero, A. Tosatto, G. Merli, D. De Stefani, L. Wright, G. Pallafacchina, A. Terrin, C. Mammucari, and R. Rizzuto. 2013. The mitochondrial calcium uniporter (MCU): Molecular identity and physiological roles. *J. Biol. Chem.* 288:10750–10758. http://dx.doi.org/10.1074/jbc.R112.420752

Perry, G.M., S. Tallaksen-Greene, A. Kumar, M.Y. Heng, A. Kneynsberg, T. van Groen, P.J. Detloff, R.L. Albin, and M. Lesort. 2010. Mitochondrial calcium uptake capacity as a therapeutic target in the R6/2 mouse model of Huntington's disease. *Hum. Mol. Genet.* 19:3354–3371. http://dx.doi.org/10.1093/hmg/ddq247

Pette, D., and R.S. Staron. 1997. Mammalian skeletal muscle fiber type transitions. *Int. Rev. Cytol.* 170:143–223. http://dx.doi.org/10.1016/S0074-7696(08)61622-8

Prosser, B.L., E.O. Hernández-Ochoa, R.M. Lovering, Z. Andronache, D.B. Zimmer, W. Melzer, and M.F. Schneider. 2010. S100A1 promotes action potential-initiated calcium release flux and force production in skeletal muscle. *Am. J. Physiol. Cell Physiol.* 299:C891–C902. http://dx.doi.org/10.1152/ajpcell.00180.2010

R Development Core Team. 2013. A language and environment for statistical computing. R Foundation for Statistical Computing, Vienna, Austria. Available at: http://www.r-project.org/index.html (accessed October 3, 2014).

Rasola, A., and P. Bernardi. 2007. The mitochondrial permeability transition pore and its involvement in cell death and in disease pathogenesis. *Apoptosis.* 12:815–833. http://dx.doi.org/10.1007/s10495-007-0723-y

Renganathan, M., and O. Delbono. 1998. Caloric restriction prevents age-related decline in skeletal muscle dihydropyridine receptor and ryanodine receptor expression. *FEBS Lett.* 434:346–350. http://dx.doi.org/10.1016/S0014-5793(98)01009-6

Ribchester, R.R., D. Thomson, N.I. Wood, T. Hinks, T.H. Gillingwater, T.M. Wishart, F.A. Court, and A.J. Morton. 2004. Progressive abnormalities in skeletal muscle and neuromuscular junctions of transgenic mice expressing the Huntington's disease mutation. *Eur. J. Neurosci.* 20:3092–3114. http://dx.doi.org/10.1111/j.1460-9568.2004.03783.x

Robertson, S.P., J.D. Johnson, and J.D. Potter. 1981. The time-course of Ca^{2+} exchange with calmodulin, troponin, parvalbumin, and myosin in response to transient increases in Ca^{2+}. *Biophys. J.* 34:559–569. http://dx.doi.org/10.1016/S0006-3495(81)84868-0

Robin, G., and B. Allard. 2013. Major contribution of sarcoplasmic reticulum Ca^{2+} depletion during long-lasting activation of skeletal muscle. *J. Gen. Physiol.* 141:557–565. http://dx.doi.org/10.1085/jgp.201310957

Romanick, M., L.V. Thompson, and H.M. Brown-Borg. 2013. Murine models of atrophy, cachexia, and sarcopenia in skeletal muscle. *Biochim. Biophys. Acta.* 1832:1410–1420. http://dx.doi.org/10.1016/j.bbadis.2013.03.011

Rosenberg, H., M. Davis, D. James, N. Pollock, and K. Stowell. 2007. Malignant hyperthermia. *Orphanet J. Rare Dis.* 2:21. http://dx.doi.org/10.1186/1750-1172-2-21

Ross, C.A. 2002. Polyglutamine pathogenesis: Emergence of unifying mechanisms for Huntington's disease and related disorders. *Neuron.* 35:819–822. http://dx.doi.org/10.1016/S0896-6273(02)00872-3

Rossi, A.E., and R.T. Dirksen. 2006. Sarcoplasmic reticulum: The dynamic calcium governor of muscle. *Muscle Nerve.* 33:715–731. http://dx.doi.org/10.1002/mus.20512

Rüegg, M.A., and D.J. Glass. 2011. Molecular mechanisms and treatment options for muscle wasting diseases. *Annu. Rev. Pharmacol. Toxicol.* 51:373–395. http://dx.doi.org/10.1146/annurev-pharmtox-010510-100537

Russ, D.W., J.S. Grandy, K. Toma, and C.W. Ward. 2011. Ageing, but not yet senescent, rats exhibit reduced muscle quality and sarcoplasmic reticulum function. *Acta Physiol. (Oxf.).* 201:391–403. http://dx.doi.org/10.1111/j.1748-1716.2010.02191.x

Saft, C., J. Zange, J. Andrich, K. Müller, K. Lindenberg, B. Landwehrmeyer, M. Vorgerd, P.H. Kraus, H. Przuntek, and L. Schöls. 2005. Mitochondrial impairment in patients and asymptomatic mutation carriers of Huntington's disease. *Mov. Disord.* 20:674–679. http://dx.doi.org/10.1002/mds.20373

Sassone, J., C. Colciago, G. Cislaghi, V. Silani, and A. Ciammola. 2009. Huntington's disease: The current state of research with peripheral tissues. *Exp. Neurol.* 219:385–397. http://dx.doi.org/10.1016/j.expneurol.2009.05.012

Sathasivam, K., C. Hobbs, M. Turmaine, L. Mangiarini, A. Mahal, F. Bertaux, E.E. Wanker, P. Doherty, S.W. Davies, and G.P. Bates. 1999. Formation of polyglutamine inclusions in non-CNS tissue. *Hum. Mol. Genet.* 8:813–822. http://dx.doi.org/10.1093/hmg/8.5.813

Schiaffino, S., and C. Reggiani. 2011. Fiber types in mammalian skeletal muscles. *Physiol. Rev.* 91:1447–1531. http://dx.doi.org/10.1152/physrev.00031.2010

Schneider, M.F., B.J. Simon, and G. Szücs. 1987. Depletion of calcium from the sarcoplasmic reticulum during calcium release in frog skeletal muscle. *J. Physiol.* 392:167–192.

Schuhmeier, R.P., and W. Melzer. 2004. Voltage-dependent Ca^{2+} fluxes in skeletal myotubes determined using a removal model analysis. *J. Gen. Physiol.* 123:33–52. http://dx.doi.org/10.1085/jgp.200308908

Schuhmeier, R.P., B. Dietze, D. Ursu, F. Lehmann-Horn, and W. Melzer. 2003. Voltage-activated calcium signals in myotubes loaded with high concentrations of EGTA. *Biophys. J.* 84:1065–1078. http://dx.doi.org/10.1016/S0006-3495(03)74923-6

Shao, J., and M.I. Diamond. 2007. Polyglutamine diseases: emerging concepts in pathogenesis and therapy. *Hum. Mol. Genet.* 16:R115–R123. http://dx.doi.org/10.1093/hmg/ddm213

Sharp, A.H., S.J. Loev, G. Schilling, S.H. Li, X.J. Li, J. Bao, M.V. Wagster, J.A. Kotzuk, J.P. Steiner, A. Lo, et al. 1995. Widespread expression of Huntington's disease gene (IT15) protein product. *Neuron.* 14:1065–1074. http://dx.doi.org/10.1016/0896-6273(95)90345-3

Shehadeh, J., H.B. Fernandes, M.M. Zeron Mullins, R.K. Graham, B.R. Leavitt, M.R. Hayden, and L.A. Raymond. 2006. Striatal neuronal apoptosis is preferentially enhanced by NMDA receptor activation in YAC transgenic mouse model of Huntington disease. *Neurobiol. Dis.* 21:392–403. http://dx.doi.org/10.1016/j.nbd.2005.08.001

Singh, R., G. Millman, E. Turin, L. Polisiakeiwicz, B. Lee, F. Gatti, J. Berge, E. Smith, J. Rutter, C. Sumski, et al. 2009. Increases in nuclear p65 activation in dystrophic skeletal muscle are secondary to increases in the cellular expression of p65 and are not solely produced by increases in IκB-α kinase activity. *J. Neurol. Sci.* 285:159–171. http://dx.doi.org/10.1016/j.jns.2009.06.030

Steinacker, J.M., A. Opitz-Gress, S. Baur, W. Lormes, K. Bolkart, L. Sunder-Plassmann, F. Liewald, M. Lehmann, and Y. Liu. 2000. Expression of myosin heavy chain isoforms in skeletal muscle of patients with peripheral arterial occlusive disease. *J. Vasc. Surg.* 31:443–449. http://dx.doi.org/10.1067/mva.2000.102848

Strand, A.D., A.K. Aragaki, D. Shaw, T. Bird, J. Holton, C. Turner, S.J. Tapscott, S.J. Tabrizi, A.H. Schapira, C. Kooperberg, and J.M. Olson. 2005. Gene expression in Huntington's disease skeletal muscle: a potential biomarker. *Hum. Mol. Genet.* 14:1863–1876. http://dx.doi.org/10.1093/hmg/ddi192

Strong, T.V., D.A. Tagle, J.M. Valdes, L.W. Elmer, K. Boehm, M. Swaroop, K.W. Kaatz, F.S. Collins, and R.L. Albin. 1993. Widespread expression of the human and rat Huntington's disease gene in brain and nonneural tissues. *Nat. Genet.* 5:259–265. http://dx.doi.org/10.1038/ng1193-259

Struk, A., G. Szücs, H. Kemmer, and W. Melzer. 1998. Fura-2 calcium signals in skeletal muscle fibres loaded with high concentrations of EGTA. *Cell Calcium.* 23:23–32. http://dx.doi.org/10.1016/S0143-4160(98)90071-9

Sun, J., C. Xin, J.P. Eu, J.S. Stamler, and G. Meissner. 2001. Cysteine-3635 is responsible for skeletal muscle ryanodine receptor modulation by NO. *Proc. Natl. Acad. Sci. USA.* 98:11158–11162. http://dx.doi.org/10.1073/pnas.201289098

Suzuki, M., Y. Nagai, K. Wada, and T. Koike. 2012. Calcium leak through ryanodine receptor is involved in neuronal death induced by mutant huntingtin. *Biochem. Biophys. Res. Commun.* 429:18–23. http://dx.doi.org/10.1016/j.bbrc.2012.10.107

Svensson, C., I. Morano, and A. Arner. 1997. In vitro motility assay of atrial and ventricular myosin from pig. *J. Cell. Biochem.* 67:241–247. http://onlinelibrary.wiley.com/doi/10.1002/%28SICI%291097-4644%2819971101%2967:2%3C241::AID-JCB9%3E3.0.CO;2-X/abstract

Szentesi, P., C. Collet, S. Sárközi, C. Szegedi, I. Jona, V. Jacquemond, L. Kovács, and L. Csernoch. 2001. Effects of dantrolene on steps of excitation–contraction coupling in mammalian skeletal muscle fibers. *J. Gen. Physiol.* 118:355–376. http://dx.doi.org/10.1085/jgp.118.4.355

Tang, T.S., H. Tu, E.Y. Chan, A. Maximov, Z. Wang, C.L. Wellington, M.R. Hayden, and I. Bezprozvanny. 2003. Huntingtin and huntingtin-associated protein 1 influence neuronal calcium signaling mediated by inositol-(1,4,5) triphosphate receptor type 1. *Neuron.* 39:227–239. http://dx.doi.org/10.1016/S0896-6273(03)00366-0

Tang, T.S., H. Tu, P.C. Orban, E.Y. Chan, M.R. Hayden, and I. Bezprozvanny. 2004. HAP1 facilitates effects of mutant huntingtin on inositol 1,4,5-trisphosphate-induced Ca release in primary culture of striatal medium spiny neurons. *Eur. J. Neurosci.* 20:1779–1787. http://dx.doi.org/10.1111/j.1460-9568.2004.03633.x

Tang, T.S., E. Slow, V. Lupu, I.G. Stavrovskaya, M. Sugimori, R. Llinás, B.S. Kristal, M.R. Hayden, and I. Bezprozvanny. 2005. Disturbed Ca^{2+} signaling and apoptosis of medium spiny neurons in Huntington's disease. *Proc. Natl. Acad. Sci. USA.* 102:2602–2607. http://dx.doi.org/10.1073/pnas.0409402102

Tang, T.S., C. Guo, H. Wang, X. Chen, and I. Bezprozvanny. 2009. Neuroprotective effects of inositol 1,4,5-trisphosphate receptor C-terminal fragment in a Huntington's disease mouse model. *J. Neurosci.* 29:1257–1266. http://dx.doi.org/10.1523/JNEUROSCI.4411-08.2009

Teichmann, M.D., F.V. Wegner, R.H. Fink, J.S. Chamberlain, B.S. Launikonis, B. Martinac, and O. Friedrich. 2008. Inhibitory control over Ca^{2+} sparks via mechanosensitive channels is disrupted in dystrophin deficient muscle but restored by mini-dystrophin expression. *PLoS ONE.* 3:e3644. http://dx.doi.org/10.1371/journal.pone.0003644

Timmer, J., T. Müller, and W. Melzer. 1998. Numerical methods to determine calcium release flux from calcium transients in muscle cells. *Biophys. J.* 74:1694–1707. http://dx.doi.org/10.1016/S0006-3495(98)77881-6

Toniolo, L., L. Maccatrozzo, M. Patruno, E. Pavan, F. Caliaro, R. Rossi, C. Rinaldi, M. Canepari, C. Reggiani, and F. Mascarello. 2007. Fiber types in canine muscles: myosin isoform expression and functional characterization. *Am. J. Physiol. Cell Physiol.* 292:C1915–C1926. http://dx.doi.org/10.1152/ajpcell.00601.2006

Trinh, H.H., and G.D. Lamb. 2006. Matching of sarcoplasmic reticulum and contractile properties in rat fast- and slow-twitch muscle fibres. *Clin. Exp. Pharmacol. Physiol.* 33:591–600. http://dx.doi.org/10.1111/j.1440-1681.2006.04412.x

Trottier, Y., D. Devys, G. Imbert, F. Saudou, I. An, Y. Lutz, C. Weber, Y. Agid, E.C. Hirsch, and J.L. Mandel. 1995. Cellular localization of the Huntington's disease protein and discrimination of the normal and mutated form. *Nat. Genet.* 10:104–110. http://dx.doi.org/10.1038/ng0595-104

Trushina, E., and C.T. McMurray. 2007. Oxidative stress and mitochondrial dysfunction in neurodegenerative diseases. *Neuroscience.* 145:1233–1248. http://dx.doi.org/10.1016/j.neuroscience.2006.10.056

Turner, C., and A.H. Schapira. 2010. Mitochondrial matters of the brain: the role in Huntington's disease. *J. Bioenerg. Biomembr.* 42:193–198. http://dx.doi.org/10.1007/s10863-010-9290-y

Turner, C., J.M. Cooper, and A.H. Schapira. 2007. Clinical correlates of mitochondrial function in Huntington's disease muscle. *Mov. Disord.* 22:1715–1721. http://dx.doi.org/10.1002/mds.21540

Ursu, D., R.P. Schuhmeier, and W. Melzer. 2005. Voltage-controlled Ca^{2+} release and entry flux in isolated adult muscle fibres of the mouse. *J. Physiol.* 562:347–365. http://dx.doi.org/10.1113/jphysiol.2004.073882

Varshney, A., and B.E. Ehrlich. 2003. Intracellular Ca^{2+} signaling and human disease: The hunt begins with Huntington's. *Neuron.* 39:195–197. http://dx.doi.org/10.1016/S0896-6273(03)00425-2

Viner, R.I., T.D. Williams, and C. Schöneich. 1999. Peroxynitrite modification of protein thiols: Oxidation, nitrosylation, and S-glutathiolation of functionally important cysteine residue(s) in the sarcoplasmic reticulum Ca-ATPase. *Biochemistry.* 38:12408–12415. http://dx.doi.org/10.1021/bi9909445

Wang, J.Q., Q. Chen, X. Wang, Q.C. Wang, Y. Wang, H.P. Cheng, C. Guo, Q. Sun, Q. Chen, and T.S. Tang. 2013. Dysregulation of mitochondrial calcium signaling and superoxide flashes cause mitochondrial genomic DNA damage in Huntington disease. *J. Biol. Chem.* 288:3070–3084. http://dx.doi.org/10.1074/jbc.M112.407726

Weiss, N., T. Andrianjafiniony, S. Dupré-Aucouturier, S. Pouvreau, D. Desplanches, and V. Jacquemond. 2010. Altered myoplasmic Ca^{2+} handling in rat fast-twitch skeletal muscle fibres during disuse atrophy. *Pflugers Arch.* 459:631–644. http://dx.doi.org/10.1007/s00424-009-0764-x

White, M.M., L.Q. Chen, R. Kleinfield, R.G. Kallen, and R.L. Barchi. 1991. SkM2, a Na^+ channel cDNA clone from denervated skeletal muscle, encodes a tetrodotoxin-insensitive Na^+ channel. *Mol. Pharmacol.* 39:604–608.

Yi, J., C. Ma, Y. Li, N. Weisleder, E. Ríos, J. Ma, and J. Zhou. 2011. Mitochondrial calcium uptake regulates rapid calcium transients in skeletal muscle during excitation-contraction (E-C) coupling. *J. Biol. Chem.* 286:32436–32443. http://dx.doi.org/10.1074/jbc.M110.217711

Zeron, M.M., H.B. Fernandes, C. Krebs, J. Shehadeh, C.L. Wellington, B.R. Leavitt, K.G. Baimbridge, M.R. Hayden, and L.A. Raymond. 2004. Potentiation of NMDA receptor-mediated excitotoxicity linked with intrinsic apoptotic pathway in YAC transgenic mouse model of Huntington's disease. *Mol. Cell. Neurosci.* 25:469–479. http://dx.doi.org/10.1016/j.mcn.2003.11.014

Zhou, J., J. Yi, R. Fu, E. Liu, T. Siddique, E. Ríos, and H.X. Deng. 2010. Hyperactive intracellular calcium signaling associated with localized mitochondrial defects in skeletal muscle of an animal model of amyotrophic lateral sclerosis. *J. Biol. Chem.* 285:705–712. http://dx.doi.org/10.1074/jbc.M109.041319